

ELECTRONIC STRUCTURE AND TIME OF FLIGHT  
MEASUREMENT FOR ORGANIC MOLECULES AND  
POLYMERS

**A Thesis**

Presented in Partial Fulfillment of the Requirements for the Degree Master of Science in the  
Graduate School of The Ohio State University

By

黃健耀

**Kin-Yiu WONG, B.Sc. (First Class Honours)**

\*\*\*\*\*

The Ohio State University

May 2003

Master's Examination Committee:

Prof. Arthur J. Epstein, Advisor

Prof. Dongping Zhong

Approved by

---

Advisor  
Department of Physics

## ABSTRACT

Conducting polymers and organic molecules are a class of materials which are interesting because of their unusual properties. These materials are lightweight, flexible, easily processed and inexpensive, but conduct electricity. Physicists and chemists worldwide explore these unusual properties and use these materials to fabricate electronic devices, such as light emitting diodes and transistors. This field was recognized when the 2000 Nobel Prize in chemistry was awarded to A.J. Heeger, A.G. MacDiarmid and Hideki Shirakawa for “the discovery and development of conductive polymers.” This thesis is exploring some of these interesting materials in both theory and experiment.

For theory, quantum chemical calculations are performed to address the origin of the red shift of the emitted light under forward bias in color-variable alternating-current light emitting (SCALE) devices. We found that the coulomb attraction due to protonation of pyridine rings by sulfonic acid containing polymers causes red shift in the band gap though the steric repulsion after protonation competes with the attraction. Hence we conclude that protonation at polymer-acidic polymer interfaces is responsible for the color variation in SCALE devices.

For experiment, charge carrier mobilities of two new materials, Tris-[4-(2-{4-[3,6-Bis(4-t-butylphenyl)cabazole-9-yl]phenyl}vinyl)phenyl]amine (TPA-Cz3d) and 9,10-Bis(2-{4-[5-(4-dodecyloxyphenyl)-1,3,4-oxadiazole-2-yl]phenyl}ethynyl)anthracene (ANTH-OXA6t-OC12), under different applied voltages at room temperature (~300K) are measured by the time of flight (TOF) method. The TOF photocurrents are analyzed by both Xiaoming Zou's model and Scher-Montroll model. We conclude that Scher-Montroll model is not easy to be applied to obtain quantitative values of the mobility. On the other hand, Zou's model provides a way to obtain the mobility consistently and quantitatively for comparisons of all organic materials. However, this model needs much more experimental data and agreements from some fundamental theory, such as quantum dynamics, to convince people that the mobility obtained by this model is reliable enough for quantitative applications.

## ACKNOWLEDGMENTS

I wish to express my gratitude to my advisor, Professor Arthur J. Epstein, for his excellent guidance, constant encouragement and invaluable discussions during the course of research.

I also would like to thank all the members of Epstein group for their supports and friendships, especially Xiaoming Zou, Julie Smallfield, Fang-Chi Hsu, Soon-Wook Cha, June-Hyoung Park, Young-Min Kim, Wesley Pirkle, Stephen Etzkorn, Vladimir Prigodin and Raju Nandyala.

## VITA

July 22, 1979 ..... Born – Hong Kong

June 2001 ..... B.Sc. (1<sup>st</sup> Class Honours) Physics, The Chinese University of Hong Kong, Hong Kong

July 2001 – present ..... Graduate Fellowship and Research Associate, Physics Department, The Ohio State University, Columbus, Ohio, USA

## PUBLICATIONS

Research Publication

1. K.Y. Wong, J.A.O. Smallfield, M. Fahlman, and A.J. Epstein, *Electronic State of Nitrogen Containing Polypyridine at the Interfaces with Model Sulfonic Acid Containing Polymer and Molecule*, **Synthetic Metals** **137**, 1031-1032 (2003)

## Fields of Study

Major Field: Physics

## TABLE OF CONTENTS

	Page
Abstract .....	ii
Acknowledgements .....	iv
Vita .....	v
List of Tables .....	ix
List of Figures .....	x
CHAPTER 1 Introduction.....	1
1.1 An Overview of Molecular Modeling.....	1
1.1.1 Molecular Mechanics .....	3
1.1.2 Electronic Structure Methods .....	3
1.2 An Overview of Charge Carrier Mobility .....	5
1.2.1 Mobility Measurement .....	7
CHAPTER 2 Foundations of <i>Ab Initio</i> Molecular Orbital Theory	10
2.1 The Schrödinger Equation.....	10
2.2 The Molecular Hamiltonian.....	12

2.3	Hartree-Fock (HF) Equations .....	13
2.3.1	Introduction to Variational Method.....	14
2.3.2	Slater Determinants and the Pauli Exclusion Principle.....	16
2.3.3	The Formula for the Expectation Value of Energy.....	17
2.3.4	Derivation of HF equations.....	20
2.4	Self-Consistent Field (SCF) Method.....	24
2.5	Correlation Energy .....	25
2.6	Density Functional Theory.....	26
2.6.1	Theoretical Motivation .....	26
2.6.2	Kohn-Sham (KS) Molecular Orbital Theory.....	28
2.7	Time Dependent Density Functional Theory .....	29

<b>CHAPTER 3 Electronic State of Nitrogen Containing Polypyridine</b>		
<b>at the Interfaces with Model Sulfonic Acid Containing Polymer</b>		
<b>and Molecule .....</b>		<b>31</b>
3.1	Computational Details .....	33
3.2	Results .....	33
3.3	Conclusions.....	39

<b>CHAPTER 4 Time of Flight Technique and Analysis .....</b>	<b>40</b>
4.1 Theoretical Background .....	40
4.2 Experimental Details .....	44
4.2.1 Materials Preparation .....	48
4.2.2 Experimental Setup .....	50
4.3 Scher-Montroll Model .....	51
4.4 A Proposed Model to Fit TOF Photocurrent .....	59
<b>CHAPTER 5 Time of Flight Measurement for New Materials.....</b>	<b>63</b>
5.1 TPA-Cz3d.....	64
5.2 ANTH-OXA6t-oc12.....	69
5.3 Discussions .....	74
<b>BIBLIOGRAPHY .....</b>	<b>76</b>

## LIST OF TABLES

Table 3.1 Change of KE, NE and EE for single pyridine due to protonation.....	37
Table 3.2 $\pi$ - $\pi^*$ gap and total energy for neutral and protonated dimer at 125° and 180°.....	38

## LIST OF FIGURES

Figure 1.1 Linear and bent versions of the methylene radical. ....	2
Figure 1.2 Chemical structure of PVK. ....	6
Figure 1.3 Chemical structure of TNF.....	6
Figure 3.1 Schematic diagram of SCALE device and its EL spectrum. ....	32
Figure 3.2 Fully sulfonated polyaniline (FSPAN). ....	32
Figure 3.3 Chemical structure of polypyridine.....	34
Figure 3.4 Illustration of two inter-ring torsion angle $\theta$ and $\alpha$ . ....	34
Figure 3.5 Extrapolation of calculated absorption energies of pyridine oligomers. .....	34
Figure 3.6 Frontier orbital energy levels for pyridine oligomers. ....	35
Figure 3.7 Frontier orbital energy levels and electron wavefunctions of pyridine before and after protonation. ....	36
Figure 3.8 Dimer HOMO-1 $n$ (neutral) and HOMO-17 $n$ (protonated).....	37
Figure 3.9 $\pi$ - $\pi^*$ gap and total energy for neutral and protonated dimer as a function of $\theta$ . ....	38
Figure 4.1 Effects of deep and shallow traps.....	41

Figure 4.2 Potential energy of an electron under the influence of an electric field	
$E$ .....	43
Figure 4.3 A typical experiment setup for measuring mobility using TOF.....	45
Figure 4.4 Profiler thickness measurement. ....	49
Figure 4.5 Ideal case when charges drift in a plane wave. ....	51
Figure 4.6 A typical photocurrent transient. ....	52
Figure 4.7 Density of electronic states $n(E)$ as a function of energy $E$ . ....	53
Figure 4.8 Photocurrent broadened by traps. ....	54
Figure 4.9 Schematic diagram for random walk model.....	55
Figure 4.10 A $\log(I/I_T) - \log(t/t_T)$ plot for 1:1 TNF-PVK.....	57
Figure 4.11 Schematic diagram for the line charge density $\rho(x,t)$ .....	60
Figure 5.1 Chemical structure of TPA-Cz3d. ....	63
Figure 5.2 Chemical structure of ANTH-OXA6t-OC12.....	64
Figure 5.3 TPA-Cz3d: Experimental and fitted photocurrent for 40V.....	65
Figure 5.4 TPA-Cz3d: Log-Log plot of the photocurrent for 40V.....	65
Figure 5.5 TPA-Cz3d: Experimental and fitted photocurrent for 60V.....	66
Figure 5.6 TPA-Cz3d: Log-Log plot of the photocurrent for 60V.....	66
Figure 5.7 TPA-Cz3d: Experimental and fitted photocurrent for 80V.....	67
Figure 5.8 TPA-Cz3d: Log-Log plot of the photocurrent for 80V.....	67
Figure 5.9 TPA-Cz3d: Experimental and fitted photocurrent for 100V.....	68

Figure 5.10 TPA-Cz3d: Log-Log plot of the photocurrent for 100V.....	68
Figure 5.11 ANTH-OXA6t-OC12: Experimental and fitted photocurrent for 20V. .....	69
Figure 5.12 ANTH-OXA6t-OC12: Log-Log plot of the photocurrent for 20V. ....	70
Figure 5.13 ANTH-OXA6t-OC12: Experimental and fitted photocurrent for 40V. .....	70
Figure 5.14 ANTH-OXA6t-OC12: Log-Log plot of the photocurrent for 40V. ....	71
Figure 5.15 ANTH-OXA6t-OC12: Experimental and fitted photocurrent for 60V. .....	71
Figure 5.16 ANTH-OXA6t-OC12: Log-Log plot of the photocurrent for 60V. ....	72
Figure 5.17 ANTH-OXA6t-OC12: Experimental and fitted photocurrent for 80V. .....	72
Figure 5.18 ANTH-OXA6t-OC12: Log-Log plot of the photocurrent for 80V. ....	73
Figure 5.19 ANTH-OXA6t-OC12: Experimental and fitted photocurrent for 100V. .....	73
Figure 5.20 ANTH-OXA6t-OC12: Log-Log plot of the photocurrent for 100V. ...	74

# CHAPTER 1

## INTRODUCTION

The first chapter provides introduction to both molecular modeling (section 1.1) and charge carrier mobility (section 1.2).

### 1.1 An Overview of Molecular Modeling

Science functions as a model of certain aspects of the physical universe. One of them is molecular modeling. It simulates chemical structures and reactions numerically, based on the fundamental laws of physics. It allows scientists to study chemical phenomena by running calculations on computers rather than by examining reactions and compounds experimentally. In this way, researchers are able to provide information about molecules and reactions, which is impossible or difficult to obtain through observation.

For example, methylene ( $\text{CH}_2$ ) radical. This is an extremely simple species, with just two hydrogen atoms bonded to a central atom (Figure 1.1).

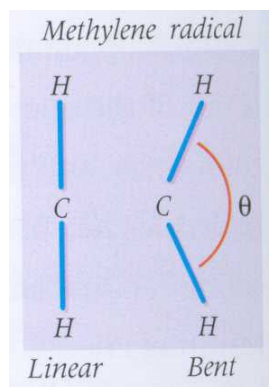


Figure 1.1 Linear and bent versions of the methylene radical.

The geometry of this radical had been investigated using both computational and experimental techniques. The early debate concentrated on the ground state of the molecule whether its geometry is linear or bent.

The first theoretical studies were performed by Foster and Frank Boys at the University of Cambridge in 1960. They concluded that the equilibrium geometry had an H-C-H angle of  $129^\circ$ . But in the following year one of the leading spectroscopists of the time, Gerhard Herzberg at the University of Ottawa, concluded from his experiments that the molecule was linear. Unfortunately for Boys, his head of department at Cambridge – Christopher Longuet – Higgins – favored an empirical approach which predicted a linear geometry. Eventually, Charles Bender and Fritz Schaefer at the University of California at Berkeley also calculated a bent geometry (with an H-C-H angle of  $135.1^\circ$ ). Soon after Bender and Schaefer's paper, several experimental research groups, including Herzberg, reported new data on the molecule showing that the molecule was indeed bent.

Consequently, molecular modeling is both an independent research area and a vital adjunct to experimental studies. There are two broad areas devoted

to the structure of molecules and their reactivity, namely molecular mechanics and electronic structure theory.

### 1.1.1 Molecular Mechanics

Molecular mechanics simulations use the laws of classical physics to predict the structures and properties of molecules. There are many different molecular mechanics methods. Each one is characterized by its particular force field. The calculations do not explicitly treat the electrons in a molecular system. Instead, they perform computations based upon the interactions among the nuclei. Electronic effects are implicitly included in force fields through parameterization.

This approximation makes molecular mechanics computations quite inexpensive computationally, and allows them to be used for very large systems containing many thousands of atoms. However, it also carries several limitations as well. For example, no force field can be generally used for all molecular systems of interest. Moreover, they are unable to describe processes which involve bond formation or bond breaking. Molecular properties which depend on subtle electronic details are also not reproducible by molecular mechanics methods.

### 1.1.2 Electronic Structure Methods

On the other hand, electronic structure methods use the laws of quantum mechanics rather than classical physics as the basis for their computations.

Quantum mechanics states that the energy and other related properties of a molecule are obtained by solving the corresponding Schrödinger equation:

$$\hat{H}\Psi = E\Psi .$$

For any but the smallest systems, however, exact solutions to the Schrödinger equation are not computationally practical. Electronic structure methods are characterized by their various mathematical approximations to its solution. There are two major classes of electronic structure methods, namely semi-empirical methods and *ab initio* methods.

#### **1.1.2.1 Semi-empirical Methods**

Semi-empirical methods use parameters obtained from experimental data to simplify the calculations. They solve an approximate form of the Schrödinger equation that depends on having appropriate parameters available for the type of the system under investigation. Different semi-empirical methods are largely characterized by their different parameter sets.

#### **1.1.2.2 Ab Initio Methods**

*Ab initio* methods use no experimental parameters in their computations. Instead, their computations are based solely on the laws of quantum mechanics --- the first principles referred to in the name *ab initio* --- and on the values of a small number of physical constants. They are the speed of light, the masses and charges of electrons and nuclei, and

Planck's constant.

In the past, *ab initio* programs were quite limited practically in the size of systems. Nowadays, due to tremendous development of powerful computers, one can compute the energies and related properties for systems containing a dozen heavy atoms on a typical workstation within just tens of minutes.

In contrast to other stated methods, *ab initio* calculations are capable of providing high quality quantitative predictions for a broad range of system. Therefore, throughout this project, we employ this method in order to investigate structural and electronic properties of some materials. The rigorous mathematical procedures of the *ab initio* molecular orbital theory are discussed in details in Chapter 2.

## 1.2 An Overview of Charge Carrier Mobility

Charge carrier motion properties are important in the applications of many organic and polymer semiconducting materials. For example, in xerography, electrostatic charges are applied to a surface of the photoreceptor film (polymer such as polyvinyl carbazole (PVK, figure 1.2) doped with trinitrofluorenone (TNF, figure 1.3), or inorganic such as amorphous Se). Charge pairs are then photo created in the photoreceptor film. A fundamental requirement for the photoreceptor is that charges can transit the medium in a time that is short compared to the time between the exposure and image development steps. Further, in organic light emitting diode (OLED), light is produced after charges

transport through some organic materials and combine with other charges with opposite signs. The voltage for operation depends on the speed of response. Moreover, in field effect transistors (FET), the reaction time also depends on the speed of the charges transport to the gate. Finally, in photovoltaics, the maximum power of the photocell is directly proportional to the photocurrent, which is in turn proportional to the charge drifting speed. For these reasons, charge transport phenomena in these technologies are of considerable importance.

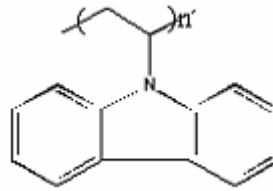


Figure 1.2 Chemical structure of PVK.

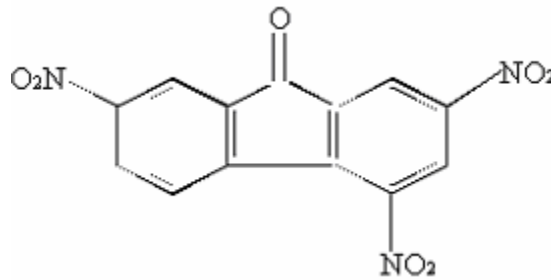


Figure 1.3 Chemical structure of TNF.

A quantity called mobility,  $\mu$ , of a carrier, as being the ratio of the drift velocity it achieves in a field  $E$  :  $v = \mu E$  , is used to describe the carrier motion in semiconducting solids. There are two extreme types of carrier motion in solids:

First one, the carriers move as a highly delocalized plane wave in a broad carrier band with a relatively large mean free path. Semiconducting crystalline inorganic materials, such as Si, Se and Ge, belong to this category, and they usually have high mobility ( $\mu \gg 1 \text{ cm}^2 / \text{Vs}$ ). Second one, the carrier is highly localized and moves by hopping from site to site, being trapped or scattered at virtually every step. Semiconducting organic and polymer materials such as poly (p-phenylenevinylene) (PPV) usually belong to this category, and are characterized by their low mobility ( $\mu \ll 1 \text{ cm}^2 / \text{Vs}$ ). Of course, there are a lot of materials falling in an intermediate category in which  $\mu \approx 10^{-3} \sim 1 \text{ cm}^2 / \text{Vs}$  and hopping motion is involved. This work is particularly interested in those organic and polymer semiconducting materials because of their potential applications in xerography, LEDs, FET and photovoltaics.

### 1.2.1 Mobility Measurement

For high mobility materials, the Hall effect provides a good method to measure the mobilities. But the measurement and interpretation of the Hall effect in low mobility materials become very difficult [1, 2, 3]. Several methods are used to measure the charge motion in low mobility materials. They include methods based on space-charge-limited current (SCLC) measurement, FET measurement, and Time-Of-Flight (TOF) measurement.

The theory of space-charge-limited current is based on the fact that any current flow through an insulator under the action of an applied field will be analogous to that of a vacuum diode. If electrons are injected into an insulator, they will travel from the injecting electrode into the conduction band of the insulator and form a space-charge similar to a vacuum diode [4]. After neglecting the contribution of diffusion to current, one can derive the following relation for a trap-free insulator,

$$J = \frac{9}{8} \varepsilon_0 \varepsilon_r \mu \frac{V^2}{d^3} \quad (1.1)$$

with  $J$  the current density,  $\varepsilon_0$  the permittivity of the vacuum,  $\varepsilon_r$  the permittivity of the sample,  $\mu$  the mobility,  $V$  the applied voltage and  $d$  the sample thickness. (1.1) is derived for one type of carrier injected from one electrode. For injection of both carriers, the current is a more complicated function of voltage and the hole and electron mobilities [4]. By measuring current dependence on voltage, one can obtain mobility by using relation (1.1). But if traps exist, an unknown factor reflecting the trapping effect has to be added to the right side of equation (1.1) [4]. This has largely limited the application of SCLC to study the transport properties of organic and polymer semiconducting materials.

Both FET and TOF are based on the same idea, i.e., to measure the transit time directly. If the measured transit time is  $t_T$ , then the average velocity  $v = d/t_T$ . And using  $E = V/d$ , one can derive the following relation,

$$\mu = \frac{d^2}{Vt_r}$$

The charges in FET are produced by the field effect at the gate electrode. Thus using FET to measure charge mobility is only limited to those materials that have pure field effect.

The drifting charges in TOF are produced using some external sources, among which laser excitation is the most widely used. But before laser was introduced, electric pulse was the main excitation source. In principle, TOF can be used to study any material that is of interest, and its interpretation is straightforward. TOF has become the standard method to measure transport phenomena in semiconducting solids.

In addition to the above techniques, other methods have been described to study charge transport properties. Thermally stimulated current methods have been described by Bässler [5], Hoshino [6], Glowacki [7] and other studies. Isothermal current decay techniques have been reported by Bässler *et al.* [8] and Samoc *et al.* [9]. These methods are generally more complex than conventional TOF, and have not been widely used. Hence in this thesis, TOF is employed to measure the mobility. The theoretical background, experimental details and models to analyze TOF photocurrent signal are discussed in details in Chapter 4.

## CHAPTER 2

# FOUNDATIONS OF *AB INITIO* MOLECULAR ORBITAL THEORY

*Ab initio* molecular orbital theory is concerned with predicting the properties of atomic and molecular systems. It is based on the fundamental laws of quantum mechanics and uses a variety of mathematical transformation and approximation techniques to solve the fundamental equations. This chapter provides a complete description of the theory underlying *ab initio* electronic structure methods.

### 2.1 The Schrödinger Equation

Quantum mechanics explains how entities like electrons have both particle-like and wave-like characteristics. The Schrödinger equation describes the wavefunction of a particle:

$$\left(-\frac{\hbar^2}{2m}\nabla^2 + V\right)\Psi(\vec{r},t) = i\hbar\frac{\partial\Psi(\vec{r},t)}{\partial t}$$

In this equation,  $\Psi$  is the wavefunction,  $m$  is the mass of the particle,  $\hbar$  is the Planck's constant over  $2\pi$ , and  $V$  is the potential field in which the particle is moving. The product of  $\Psi$  with its complex conjugate ( $\Psi^*\Psi$ , often written as  $|\Psi|^2$ ) is interpreted as the probability distribution of the particle.

The Schrödinger equation for a collection of particles like a molecule is very similar. In this case the  $\Psi$  would be a function of the coordinates of all the particles in the system as well as  $t$ .

The energy and many other properties of the particle can be obtained by solving the Schrödinger equation for  $\Psi$ , subject to the appropriate boundary conditions. Many possible wavefunctions are solutions to it, corresponding to different states of the system.

If  $V$  is not a function of time, the Schrödinger equation can be simplified using the mathematical technique known as separation of variables. Then we obtain two equations, one of which depends on the position of the particle independent of time and the other of which is a function of time alone:

$$\begin{aligned}\Psi(\vec{r}, t) &= \psi(\vec{r})f(t) \\ \Rightarrow \frac{d}{dt}f(t) &= Ef(t), \text{ and} \\ \Rightarrow \left(-\frac{\hbar^2}{2m}\nabla^2 + V(\vec{r})\right)\psi(\vec{r}) &= E\psi(\vec{r})\end{aligned}$$

The latter one is known as the familiar time-independent Schrödinger equation.

The various solutions to the time-independent Schrödinger equation correspond to different stationary states of the particle. The one with the lowest energy is called ground state.

## 2.2 The Molecular Hamiltonian

In practice, one usually does not use the complete Hamiltonian for an isolated molecular system. The complete Hamiltonian includes nuclear and electronic kinetic energy operators, electrostatic interactions among all charged particles, and interactions among all magnetic moments due to spin and orbital motions of nuclei and electrons. Actually a moving particle experiences a change in mass due to relativistic effects should be included in the complete Hamiltonian. Hence, the resulting Hamiltonian is much too complicated to work with.

Usually, relativistic mass effects are ignored, the Born-Oppenheimer approximation is made to remove nuclear kinetic energy since the mass of nucleus is thousands of times greater than that of an electron such that we assume nuclei are so slow-moving relative to electrons that we may regard them as fixed masses, and all magnetic interactions are ignored except in special cases where we are interested in spin coupling. We are allowed to ignore all of them because these approximations are good enough to compute energy in at least 0.1% accuracy. Consequently, the resulting Hamiltonian for the molecular

system is solely the sum of the electronic energy and the nuclear repulsion energy:

$$\text{The electronic energy is } \hat{H} = -\frac{1}{2} \sum_{i=1}^n \nabla_i^2 - \sum_{\mu=1}^N \sum_{i=1}^n \frac{Z_{\mu}}{r_{\mu i}} + \sum_{i=1}^{n-1} \sum_{j=i+1}^n \frac{1}{r_{ij}},$$

$$\text{the nuclear repulsion energy is } V = \sum_{\mu=1}^{N-1} \sum_{\nu=\mu+1}^N \frac{Z_{\mu} Z_{\nu}}{r_{\mu\nu}}.$$

where  $i$  and  $j$  are indices for the  $n$  electrons, whereas  $\mu$  and  $\nu$  are indices for the  $N$  nuclei.

Both are written in atomic units. The atomic unit of length is the Bohr radius:

$$a_0 = \frac{(4\pi\epsilon_0)\hbar^2}{m_e e^2} = 0.52917725 \text{ \AA}$$

Energies are measured in hartrees, defined as the Coulomb repulsion between two electron separated by 1 bohr:

$$1 \text{ hartree} = \frac{e^2}{(4\pi\epsilon_0)a_0} = 27.211eV$$

Masses are also specified in terms of electron mass units (i.e. define  $m_e = 1$ )

We shall use these units in all future equations

## 2.3 Hartree-Fock (HF) Equations

*The underlying physical laws necessary for the mathematical theory of a large part of physics and the whole of chemistry are thus completely known, and*

*the difficulty is only that the exact application of these laws leads to equations much too complicated to be soluble.* --- P. A. M. Dirac, 1929 [10]

Although, we have made several approximations to simplify the molecular Hamiltonian, it is not possible to solve it analytically for any but the most trivial molecular systems. This is because the equation is not separable. Fortunately, there are approximate methods that can be used to solve it to almost any accuracy desired, once providing necessary CPU resources. In this section, we discuss one of the most widely used methods, variational method, and show how it leads to Hartree-Fock equations.

### 2.3.1 Introduction to Variational Method

First we know that the eigenfunctions, say  $\psi_n$ , of any quantum mechanical operator, say  $\hat{H}$ , corresponding to an observable variable, say energy  $E_n$ , constitute an orthonormal complete set. The ground state  $\psi_0$  has the lowest energy  $E_0$ . If  $\psi_0$  is not known, we approximate it by a trial wavefunction  $\phi_0$ . Let  $\phi_0$  satisfies the same boundary conditions as  $\psi_0$  does and choose  $\phi_0$  such that  $\langle \phi_0 | \phi_0 \rangle = 1$ . Since  $\psi_n$  forms an orthonormal complete set, we are able to express  $\phi_0$  in terms of  $\psi_n$ :

$$\phi_0 = \sum_{k=0}^{\infty} c_k \psi_k .$$

By calculating the scalar product of  $\phi_0$ , we obtain:

$$\sum_{j=0}^{\infty} |c_j|^2 = 1$$

Thus, the average energy from the trial function  $\phi_0$  is given by:

$$\Rightarrow \langle \phi_0 | \hat{H} | \phi_0 \rangle = \sum_{j=0}^{\infty} |c_j|^2 E_j$$

$$\Rightarrow \langle \phi_0 | \hat{H} | \phi_0 \rangle \geq E_0.$$

It gives an upper bound for  $E_0$ . Thus, to obtain a good estimate for  $E_0$ , we try to minimize  $\langle \phi_0 | \hat{H} | \phi_0 \rangle$  as far as possible. Usually the trial function  $\phi_0$  depends on a number of parameters, which are varied until the expectation value of H is a minimum.

As a specific example, consider a particle in a one-dimensional box. Even without prior knowledge of the exact ground state wavefunction, we expect it to be symmetric about  $x = a/2$  and go to zero at the walls. One of the simplest functions with this symmetry is  $x^n(x-a)^n$  where n is an integer. Therefore let us estimate  $E_0$  by using:

$$\phi = c_1 x(a-x) + c_2 x^2(a-x)^2$$

as a trial function, where  $c_1$  and  $c_2$  are to be determined variationally. After a straightforward calculation, we find that

$$E_{\min} = 0.125002 \frac{h^2}{ma^2}$$

compared to

$$E_{exact} = \frac{h^2}{8ma} = 0.125000 \frac{h^2}{ma^2}.$$

So we see that using a quite reasonable function can produce impressive result. In fact, one can show a first order error in the trial function as an estimate of  $\psi_0$  gives a second order error for estimating  $E_0$ .

### 2.3.2 Slater Determinants and the Pauli Exclusion Principle

We now come to a position to guess a good trial wavefunction for a real molecular system. Molecular orbital theory decomposes the total wavefunction  $\Psi$  into a combination of Molecular Orbitals (MO):  $\phi_n$ . We choose a Linear Combination of Atomic Orbitals (LCAO) to form MO. The MO's are normalized and mutually orthogonal. The simplest possible way of constructing the many-body wavefunction  $\Psi$  is by forming a Hartree-product:

$$\Psi(\vec{r}) = \prod_{i=1}^n \phi_i(\vec{r}).$$

However, according to the Pauli Exclusion Principle,  $\Psi$  must be antisymmetric under the interchange of any two electrons so that there are no more than one electrons have the same values of all quantum numbers. Hence, the Hartree-product is an inadequate wavefunction since it not antisymmetric.

It was pointed out by Slater [11] that there is a simple way to write a wavefunction guaranteeing that it would be antisymmetric: One writes the wavefunction  $\Psi$  as a determinant. It is known as a Slater determinant:

$$\frac{1}{\sqrt{N!}} \begin{vmatrix} \phi_1(1) & \phi_1(2) & \phi_1(3) & \cdots & \cdots & \phi_1(N) \\ \phi_2(1) & \phi_2(2) & \phi_2(3) & \cdots & \cdots & \phi_2(N) \\ \phi_3(1) & \phi_3(2) & \phi_3(3) & \cdots & \cdots & \phi_3(N) \\ \vdots & & & \ddots & & \\ \vdots & & & & \ddots & \\ \phi_N(1) & \phi_N(2) & \phi_N(3) & \cdots & \cdots & \phi_N(N) \end{vmatrix},$$

where  $N$  is the number of electrons.

The shorthand formula for a Slater determinant is:

$$\frac{1}{\sqrt{N!}} |\phi_1(1)\phi_2(2)\phi_3(3)\cdots\phi_N(N)|.$$

### 2.3.3 The Formula for the Expectation Value of Energy

In this part, we derive the expression for the expectation value  $\bar{E} = \langle \Psi | \hat{H} | \Psi \rangle$  for the case in which  $\Psi$  is a single Slater determinant.

First, we limit the discussion to the case in which  $\Psi$  is a closed-shell determinant. We shall illustrate our arguments by referring to a four-electron example:

$$\Psi_4 = \frac{1}{\sqrt{4!}} |\phi_1(1)\bar{\phi}_1(2)\phi_2(3)\bar{\phi}_2(4)|,$$

where  $\bar{\phi}_n$  is the spin down of  $\phi_n$ .

Upon expanding  $\langle \Psi_4 | \hat{H} | \Psi_4 \rangle$ , we obtain a set of 4! products on both the left and right hand sides of  $\hat{H}$  :

$$\bar{E} = \frac{1}{4!} \left\{ \int \phi_1^*(1) \bar{\phi}_1^*(2) \phi_2^*(3) \bar{\phi}_2^*(4) \hat{H} | \phi_1(1) \bar{\phi}_1(2) \phi_2(3) \bar{\phi}_2(4) | d\tau - \int \phi_1^*(1) \bar{\phi}_1^*(4) \phi_2^*(3) \bar{\phi}_2^*(2) \hat{H} | \phi_1(1) \bar{\phi}_1(2) \phi_2(3) \bar{\phi}_2(4) | d\tau + \dots \right\}$$

In this expression,  $\bar{E}$  is a sum of 4! integrals, each containing one term from the set of the left of  $\hat{H}$  and all 4! from the set of the right.

At the first glance, it might seem that we must evaluate all of the 4! integrals. But it can be shown easily that these integrals, times +1 or -1 coefficients, are all equal to each other, enabling us to write  $\bar{E}$  as 4! times the first integrals:

$$\bar{E} = \int \phi_1^*(1) \bar{\phi}_1^*(2) \phi_2^*(3) \bar{\phi}_2^*(4) \hat{H} | \phi_1(1) \bar{\phi}_1(2) \phi_2(3) \bar{\phi}_2(4) | d\tau.$$

Recall the Hamiltonian  $\hat{H}$  is:

$$\hat{H} = \sum_{i=1}^4 \left( -\frac{1}{2} \nabla_i^2 - \sum_{\mu=1}^{nuclei} \frac{Z_\mu}{r_{\mu i}} \right) + \sum_{i=1}^3 \sum_{j=i+1}^4 \frac{1}{r_{ij}}$$

$$\Rightarrow \hat{H} = \sum_{i=1}^4 H_i^{core} + \sum_{\substack{double \\ sum}} \frac{1}{r_{ij}}.$$

We see that  $\hat{H}$  is comprised of one-electron operators,  $H_i^{core}$ , and two-electron operators for inter-electronic repulsion. Consider first the one-

electron integrals. Using the orthogonal properties of  $\phi_n$ , it is not difficult to show that:

$$\langle \Psi_4 | \sum_{i=1}^4 H_i^{core} | \Psi_4 \rangle = \sum_{i=1}^4 2H_{ii}, \text{-----(1)}$$

where  $H_{ii} = \int \phi_i^*(1) H_1^{core} \phi_i(1) d\tau_1$ .

We now turn to integrals containing two-electron operators. Since the operator  $\frac{1}{r_{ij}}$  and MOs commute, and  $\phi_n$  orthogonal to each other, it is

straightforward to show that:

$$\langle \Psi_4 | \sum_{\substack{\text{double} \\ \text{sum}}} \frac{1}{r_{ij}} | \Psi_4 \rangle = J_{11} + 4J_{12} - 2K_{12} + J_{22}, \text{-----(2)}$$

where  $J_{ij} = \langle \phi_i(1)\phi_j(2) | \frac{1}{r_{12}} | \phi_i(1)\phi_j(2) \rangle$ ,

$K_{ij} = \langle \phi_i(1)\phi_j(2) | \frac{1}{r_{12}} | \phi_i(2)\phi_j(1) \rangle$ .

$J_{ij}$  is known as a coulomb integral, because  $J_{ij}$  can be rearranged to give:

$$J_{ij} = \int \phi_j^*(2) \int \phi_i^*(1) \frac{1}{r_{12}} \phi_i(1) d\tau_1 \phi_j(2) d\tau_2$$

It can be interpreted classically as two mutually repelling charge clouds.

On the other hands,  $K_{ij}$  could not be explained classically. It is called an exchange integral. Note that if we use Hartree-product to be the trial

wavefunction instead, we would not come across the exchange integral.

In fact,  $K_{ij}$  is a consequence of the Pauli Exclusion Principle.

Adding (1) to (2), we find the formula for the expectation value of  $\bar{E}$  :

$$\bar{E} = \langle \Psi_4 | \hat{H} | \Psi_4 \rangle = \sum_{i=1}^2 2H_{ii} + \sum_{i=1}^2 \sum_{j=1}^2 (2J_{ij} - K_{ij}).$$

Note:  $J_{ij} = J_{ji}$ ,  $K_{ij} = K_{ji}$  and  $J_{ii} = K_{ii}$ .

Generalizing to the 2n-electron, closed-shell case:

$$\bar{E} = \langle \Psi_{2n} | \hat{H} | \Psi_{2n} \rangle = 2 \sum_{i=1}^n H_{ii} + \sum_{i=1}^n \sum_{j=1}^n (2J_{ij} - K_{ij}).$$

This is the desired expression for  $\bar{E}$  in terms of MOs, for a single Slater determinant, closed shell wavefunction.

### 2.3.4 Derivation of HF equations

To find the best MOs, we seek small variations  $\delta\phi$  that minimize  $\bar{E}$ . But there is a restriction in the variations  $\delta\phi$ . The MOs can only be varied in ways that do not destroy their orthonormality. Thus, we may write that, at the minimum  $\bar{E}$  :

$$\bar{E} - 2 \sum_i \sum_j \varepsilon_{ij} S_{ij} = \text{constant for } \delta\phi \text{ -----(3)}$$

where  $S_{ij} = \langle \phi_i | \phi_j \rangle$ .

We use a technique, known as “Lagrange’s method of undetermined multipliers” to solve  $\varepsilon_{ij}$ . These Lagrangian multipliers will ultimately turn out to be essentially the MO energies.

The stability of the quantity on the left-hand side of (3) may be expressed as:

$$2\sum_{i=1}^n \delta H_{ii} + \sum_{i=1}^n \sum_{j=1}^n (2\delta J_{ij} - \delta K_{ij}) - 2\sum_i \sum_j \varepsilon_{ij} \delta S_{ij} = 0 \text{-----(4)}.$$

The variations occur in the MOs  $\phi$ , and so:

$$\delta S_{ij} = \langle \delta \phi_i | \phi_j \rangle + \langle \phi_i | \delta \phi_j \rangle,$$

$$\delta H_{ii} = \langle \delta \phi_i(1) | H_1^{core} | \phi_i(1) \rangle + \langle \phi_i(1) | H_1^{core} | \delta \phi_i(1) \rangle,$$

$$\delta J_{ij} = \langle \delta \phi_i(1) \phi_j(2) | \frac{1}{r_{12}} | \phi_i(1) \phi_j(2) \rangle + \langle \phi_i(1) \delta \phi_j(2) | \frac{1}{r_{12}} | \phi_i(1) \phi_j(2) \rangle$$

+ complex conjugates,

$$\delta K_{ij} = \langle \delta \phi_i(1) \phi_j(2) | \frac{1}{r_{12}} | \phi_i(2) \phi_j(1) \rangle + \langle \phi_i(1) \delta \phi_j(2) | \frac{1}{r_{12}} | \phi_i(2) \phi_j(1) \rangle$$

+ complex conjugates.

It is convenient to define a coulomb operator  $\hat{J}_i(1)$  as:

$$\hat{J}_i(1) = \langle \phi_i(2) | \frac{1}{r_{12}} | \phi_i(2) \rangle.$$

Using this definition we can rewrite  $\delta J_{ij}$  as:

$$\delta J_{ij} = \langle \delta \phi_i(1) | \hat{J}_j(1) | \phi_i(1) \rangle + \langle \delta \phi_j(1) | \hat{J}_i(1) | \phi_j(1) \rangle + \text{complex conjugates.}$$

In the same spirit, we define an exchange operator  $\hat{K}_i(1)$ , which, because it involves an orbital exchange, must be written in the context of an orbital being operated on:

$$\hat{K}_i(1)\phi_j(1) = \langle \phi_i(2) | \frac{1}{r_{12}} | \phi_j(2) \rangle \phi_i(1).$$

This enables us to write  $\delta K_{ij}$  as:

$$\delta K_{ij} = \langle \delta \phi_i(1) | \hat{K}_j(1) | \phi_i(1) \rangle + \langle \delta \phi_j(1) | \hat{K}_i(1) | \phi_j(1) \rangle + \text{complex conjugates.}$$

Employing the operators  $\hat{J}_i(1)$  and  $\hat{K}_i(1)$ , (4) can be written as follows:

$$\begin{aligned} & 2 \sum_i \{ \langle \delta \phi_i(1) | H_1^{core} + \sum_j (2\hat{J}_j(1) - \hat{K}_j(1)) | \phi_i(1) \rangle - \sum_j \varepsilon_{ij} \phi_j(1) \} + \\ & 2 \sum_i \{ \langle \phi_i(1) | H_1^{core} + \sum_j (2\hat{J}_j(1) - \hat{K}_j(1)) | \delta \phi_i(1) \rangle - \sum_j \varepsilon_{ji} \phi_j^*(1) \} = 0 \end{aligned} \quad \text{-----(5)}$$

Here we have made use of the Hermitian properties of  $H^{core}$ ,  $\hat{J}$  and  $\hat{K}$ .

$\delta \phi_i$  and  $\delta \phi_i^*$  are independent of each other. So from (5), we obtain:

$$\begin{aligned} [H_1^{core} + \sum_j (2\hat{J}_j(1) - \hat{K}_j(1))] \phi_i(1) &= \sum_j \varepsilon_{ij} \phi_j(1) \\ [H_1^{core} + \sum_j (2\hat{J}_j(1) - \hat{K}_j(1))] \phi_i^*(1) &= \sum_j \varepsilon_{ji} \phi_j^*(1) \end{aligned} \quad \text{-----(6)}$$

Taking the complex conjugate of the second one of (6), and subtracting it from the first one, we find:

$$\sum_j (\varepsilon_{ij} - \varepsilon_{ji}^*) \phi_j(1) = 0$$

$$\Rightarrow \varepsilon_{ij} = \varepsilon_{ji}^*$$

It implies  $\varepsilon_{ij}$  is the element of an Hermitian matrix.

Let  $\hat{F}(1) = H_1^{core} + \sum_j (2\hat{J}_j(1) - \hat{K}_j(1))$ , where  $\hat{F}$  is known as Fock operator.

Then (6) can be summarized as:

$$\hat{F}(1)\phi_i(1) = \sum_j \varepsilon_{ij}\phi_j(1) \text{ .------(7)}$$

A transformation that mixes the MOs  $\phi$  without affecting the property of orthonormality is called a unitary transformation. Let  $U$  stand for such a transformation. We have a transformed set of  $\phi$  called  $\phi'$  is given by:

$$\phi_i' = \sum_j U_{ji}\phi_j$$

In matrix notation, this is:

$$\tilde{\phi}' = \tilde{\phi}\tilde{U}$$

where  $\tilde{\phi}'$  and  $\tilde{\phi}$  are row vectors:

$$\tilde{\phi} = (\phi_1, \phi_2, \phi_3 \cdots \phi_n)$$

$$\tilde{\phi}' = (\phi_1', \phi_2', \phi_3' \cdots \phi_n')$$

and  $\tilde{U}$  is an  $n \times n$  matrix, with

$$\tilde{U}\tilde{U}^+ = \tilde{U}^+\tilde{U} = 1.$$

In terms of these matrices, (7) is:

$$\hat{F}\tilde{\phi} = \tilde{\phi}\tilde{E},$$

where  $\tilde{E}$  is an  $n \times n$  Hermitian matrix. If we multiply this from the right by  $\tilde{U}$ , gives:

$$\begin{aligned}\hat{F}\tilde{\phi}\tilde{U} &= \tilde{\phi}\tilde{E}\tilde{U} \\ \Rightarrow \hat{F}\tilde{\phi}\tilde{U} &= \tilde{\phi}\tilde{U}\tilde{U}^+\tilde{E}\tilde{U} . \\ \Rightarrow \hat{F}\tilde{\phi}' &= \tilde{\phi}'\tilde{U}^+\tilde{E}\tilde{U}\end{aligned}$$

Since  $\tilde{E}$  is a Hermitian matrix, we can require that the matrix  $\tilde{U}$  be such that  $\tilde{U}^+\tilde{E}\tilde{U}$  is a diagonal matrix  $\tilde{E}'$ . This requirement defines  $\tilde{U}$ , and we have:

$$\hat{F}\tilde{\phi}' = \tilde{\phi}'\tilde{E}',$$

which corresponds to:

$$\hat{F}\phi'_i = \varepsilon_i \phi'_i \text{ .-----(8)}$$

This equation is commonly referred to be the HF equation.

## 2.4 Self-Consistent Field (SCF) Method

Using HF equations, we are able to reduce the complex many-body molecular system to be one-body problem, as it is revealed by (8). It is similar to the problem of a particle in a box, which was illustrated in the section 2.3.1, but now the Fock operator itself is a function of the trial MOs. Thus, we have to

make an initial guess of the MOs first in order to obtain the initial Fock operator. Then just using the same method as that of a particle in a box (seeking best MOs to minimize the energy), we can solve for a new set of MOs. Next, construct a new Fock operator by this new set of MOs, and repeats the process once again. The operation is repeated until the values of MOs are converged or self-consistent. This approach is named as the Self-Consistent Field (SCF) method.

## 2.5 Correlation Energy

The HF energy is not as low as the true energy of the system. This is because the wavefunction is solely a linear combination of products of functions of independent coordinates. Physically, this corresponds to say that the probability for finding an electron in  $d\tau_1$  at some instant is not influenced by the presence or absence of another electron in some nearby element  $d\tau_2$  at the same instant. This is consistent with the fact that the Fock operator treats each electron as though it were moving in the time-averaged potential field due to the other electrons, no matter what locations of others.

However, in reality, their motions are correlated. Although, since the HF wavefunction is antisymmetric, it automatically includes the major correlation effects arising from pairs of electrons with the same spin (exchange correlation), the motion of electrons of opposite spin remains uncorrelated under HF theory, however. For example, in a real system there are some locations where other electrons do not likely to be, though effectively they would produce the same

time-averaged potential field. This is because the mutual repulsion of their negative charges would cause a tendency for them to keep out each other's way. Thus, the HF wavefunctions is formally incapable of describing these correlated motions and the HF energy is higher than the true energy. The energy difference between the HF and the "real" energy for a system is referred as the correlation energy.

## 2.6 Density Functional Theory

The major premise of density functional theory (DFT) is the energy of an electronic system can be represented as some mathematical form of the electron density. DFT dates back to Thomas [12] (1927), Fermi [13] (1928) and Dirac [14] (1930). It is not a newcomer to the field, but it has been less popular until recently. We shall see why later.

### 2.6.1 Theoretical Motivation

We may take advantage of our knowledge of quantum mechanics in asking about what particular physical observable might be useful. Having gone through the exercise of constructing the Hamiltonian operator and showing the utility of its eigenfunctions, it would be sufficient to our task simply to find a physical observable that permitted the a priori construction of the Hamiltonian operator. What then is needed? The molecular Hamiltonian depends only on the positions and atomic numbers

of the nuclei and the total number of electrons. The dependence on total number of electrons immediately suggests that a useful physical observable would be the electron density  $\rho$ , since, integrated over all space, it gives the total number of electron  $N$ , i.e.,

$$N = \int \rho(\mathbf{r}) d\mathbf{r}$$

So one can express the electronic energy,  $E_{el}$ , in terms of the electron density instead of the wavefunction:

$$E_{el} = -\frac{1}{2} \sum_i^{electrons} \int \phi_i(\mathbf{r}) \nabla^2 \phi_i(\mathbf{r}) d\mathbf{r} + \sum_a^{nuclei} \int \frac{Z_a}{|\mathbf{r}_a - \mathbf{r}|} \rho(\mathbf{r}) d\mathbf{r} + \frac{1}{2} \int \frac{\rho(\mathbf{r}_1) \rho(\mathbf{r}_2)}{|\mathbf{r}_1 - \mathbf{r}_2|} d\mathbf{r}_1 d\mathbf{r}_2 + E_{XC}$$

where the first term represents the kinetic energy of the  $N$  electrons, the second term is the nuclear-electron attraction, the third term is the coulomb interaction between two charge distributions  $\rho(\mathbf{r}_1)$  and  $\rho(\mathbf{r}_2)$  – typically called the  $J$  integrals and the fourth term is the exchange-correlation energy.

For HF theory, the  $E_{XC}$  term just included quantum mechanical exchange (see the  $K$  integrals in section 2.3.3). In DFT, we can now suggest other methods to include the exchange-correlation functional (function of a function), and all of this “operates” on the electron density  $\rho$ .

## 2.6.2 Kohn-Sham (KS) Molecular Orbital Theory

The discussion above has emphasized that the density determines the external potential which determines the Hamiltonian, which determines the wavefunction. And, of course, with the Hamiltonian and wavefunction in hand, the energy can be computed. However, if one attempts to proceed in this direction there is no simplification over molecular orbital theory, since the final step is still solution of the Schrödinger equation, and this is prohibitively difficult in most instances. The difficulty derives from the electron-electron interaction term in the correct Hamiltonian. In a key breakthrough, Kohn and Sham [15] (1965) realized that things would be considerably simpler if only the Hamiltonian operator were one for a non-interacting system of electrons (Kohn shared the 1998 Nobel Prize in Chemistry for “his development of the density functional theory”). Such a Hamiltonian can be expressed as a sum of one-electron operators, has eigenfunctions that are Slater determinants of the individual one-electron eigenfunctions and has eigenvalues that are simply the sum of the one-electron eigenvalues. And the KS equation looks very similar to the HF equation:

$$\left[ -\frac{1}{2} \nabla_i^2 + \sum_a^{\text{nuclei}} \frac{Z_a}{|\mathbf{r}_a - \mathbf{r}_1|} + \int \frac{\rho(\mathbf{r}_2)}{|\mathbf{r}_1 - \mathbf{r}_2|} d\mathbf{r}_2 + V_{XC} \right] \phi_i(\mathbf{r}_1) = \varepsilon_i \phi_i(\mathbf{r}_1)$$

where the exchange-correlation potential  $V_{XC}$  is represented by an energy derivative with regard to the electron density  $\rho$

$$V_{xc}[\rho] = \frac{\delta E_{xc}[\rho]}{\delta \rho}$$

So all of the terms are “straightforward” to evaluate, except for *what is the exchange-correlation functional?* There are many suggestions to approximate the functional. One of the most popular one, B3LYP [16] was employed throughout this thesis.

## 2.7 Time Dependent Density Functional Theory

If a molecule is subjected to a linear electric field  $\mathbf{E}$  that is fluctuating such that:

$$\mathbf{E} = \mathbf{r} \cos(\omega t)$$

where  $\mathbf{r}$  is the position vector in one dimension,  $t$  is time and  $\omega$  is the frequency of the fluctuation, it can be shown that the frequency-dependent polarizability is well approximated by:

$$\langle \alpha \rangle_{\omega} = \sum_{i \neq 0}^{\text{states}} \frac{|\langle \psi_0 | \mathbf{r} | \psi_i \rangle|^2}{\omega - (E_i - E_0)}$$

where the numerator of each term in the sum is a so-called transition dipole moment and the denominator involves the frequency and the energies of the excited states and the ground state. Note that, if the frequency corresponds exactly to the difference in energy between an excited state and the ground state, there is a pole in the frequency-dependent polarizability, i.e., it diverges since the denominator goes to zero.

Using propagator methodology (sometimes also called a Green's function approach or an equation-of-motion method), the poles of the frequency-dependent polarizability can be determined without having to compute all of the necessary excited-state wave functions and their corresponding state energies. The necessary matrix equations are quite complex and only a qualitative summary is provided here. Within the confines of the so-called random-phase approximation (RPA) the integrals that are required to compute the excitation energies are essentially those required to fill the CI matrix containing all single and double excitations and the transition dipole moments between the ground state and all singly excited configurations.

A DFT method that is strongly analogous to RPA is called time-dependent DFT (TDDFT). In this case, the KS orbital energies and various exchange integrals are used in place of matrix elements of the Hamiltonian. TDDFT is usually most successful for low-energy excitations, because the KS orbital energies for orbitals that are high up in the virtual manifold are typically quite poor. Casida, Casida, and Salahub (1998) [17] have suggested that TDDFT results are most reliable if the following two criteria are met: (i) the excitation energy should be significantly smaller than the molecular ionization potential (not that excitations from occupied orbitals below the HOMO are allowed, so this is not a tautological condition) and (ii) promotion(s) should not take place into orbitals having positive KS eigenvalues. In this thesis, TDDFT was employed to find excited states.

## CHAPTER 3

# ELECTRONIC STATE OF NITROGEN CONTAINING POLYPYRIDINE AT THE INTERFACES WITH MODEL SULFONIC ACID CONTAINING POLYMER AND MOLECULE

The original polymeric light emitting diode (LED) design utilized polymers such as poly(p-phenylenevinylene) as the light emitting material sandwiched between two dissimilar metallic contacts and operated under forward bias only [18]. An alternative design based upon the concept of a bipolar-driven LED, incorporating two “encapsulation” layers surrounding the light emitting polymer layer, is the so-called symmetrically configured alternating current light emitting (SCALE) device (figure 3.1) [19]. Color variable SCALE devices were later fabricated by replacing one of the “encapsulation” layers with a conducting fully sulfonated polyaniline (FSPAN) (figure 3.2) [20]. The origin of the red shift of the emitted light that occurs under forward bias (figure 3.1) in such devices was

proposed as protonation of the pyridine nitrogen near the interface by the sulfonic acid containing FSPAN. In the previous work [21], X-ray photoelectron spectroscopy (XPS) was used to show protonation at the interface does indeed occur. In this study, DFT is employed to investigate the origin of the red shift after protonation.

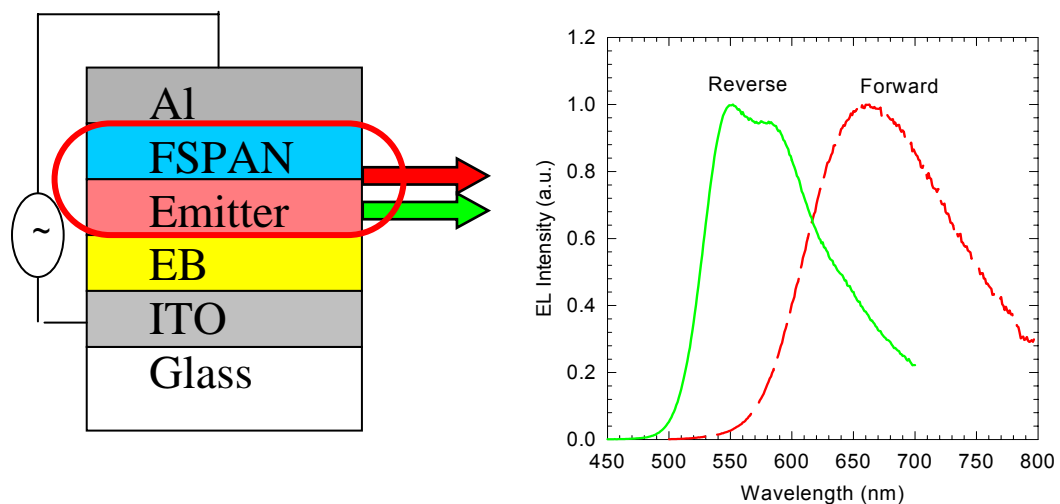


Figure 3.1 Schematic diagram of SCALE device and its EL spectrum.

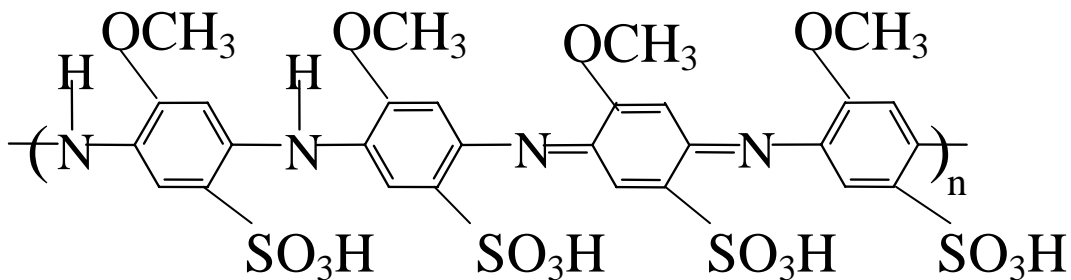


Figure 3.2 Fully sulfonated polyaniline (FSPAN).

### 3.1 Computational Details

All the calculations were performed using Gaussian 98 [22]. The ground state structure was optimized at the restricted Hartree-Fock (HF) level. DFT was applied to find the ground state energy and Kohn-Sham molecular orbital at B3LYP level. The total energy of the singlet excited state ( $\pi\pi^*$ ) was determined by time-dependent DFT. The vertical absorption energy was calculated as the difference between the ground state energy and the excited state energy. 6-31G(d) was the basis set for all calculations.

### 3.2 Results

Protonation of polypyridine (PPy) (figure 3.3) also has been studied theoretically. Here we have used PPy oligomers, PY $m$ HH, where  $m$  refers to the number of pyridine rings and HH (Head-to-Head) means the neighboring rings alternate in orientation. Two inter-ring torsion angles,  $\theta$  and  $\alpha$ , are defined in figure 3.4.  $\theta$  of PY2, PY4, PY6 and PY8 are all 180°.  $\alpha$  of PY4, PY6 and PY8 are -136°, 136°, and -136° respectively. Absorption energy of PPy is obtained by the y-intercept of the extrapolation of the calculated absorption energies of oligomers:  $E_{\text{oligomer}} = E_{\text{polymer}} + A/m$ , where  $A$  is a constant (figure 3.5). The value of y-intercept ( $E_{\text{polymer}}$ ) is 3.38 eV and in sound agreement with the observed gap ~3.1-3.3 eV [23].

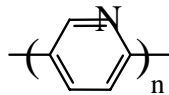


Figure 3.3 Chemical structure of polypyridine.

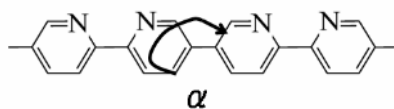
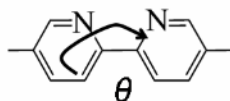


Figure 3.4 Illustration of two inter-ring torsion angle  $\theta$  and  $\alpha$ . Both structures are sketched for  $\theta$  and  $\alpha$  at zero value.

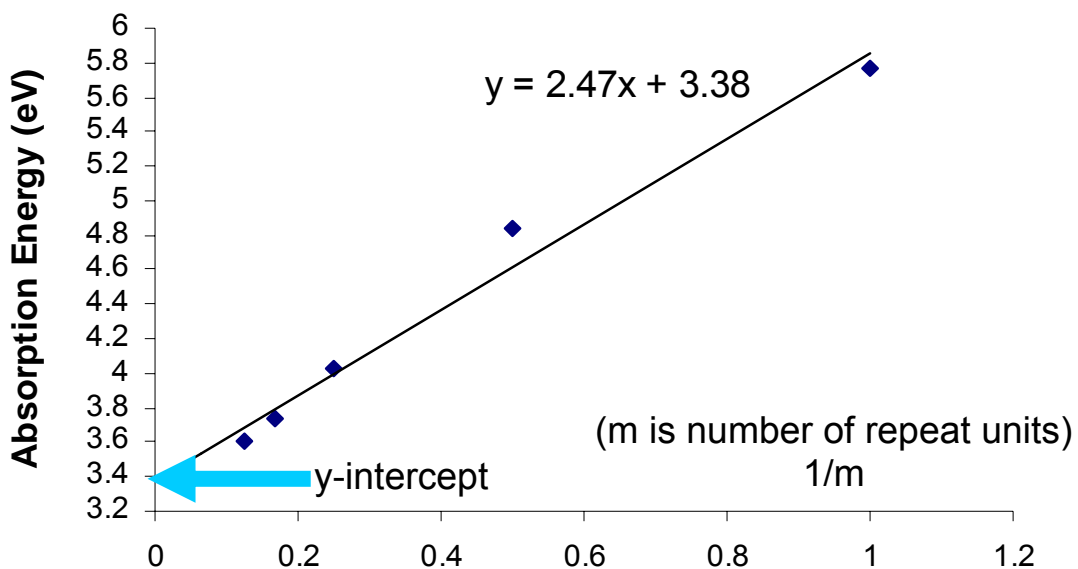


Figure 3.5 Extrapolation of calculated absorption energies of pyridine oligomers.

Further, the phenomena that  $n$  orbital (non-bonding MO) remains relatively unaffected in energy as the conjugation length increases while  $\pi$ - $\pi^*$  energy gap decreases and the highest occupied  $\pi$  orbital crosses  $n$  orbital from PY1 to PY2 agree with exciplex experimental results (figure 3.6) [24].

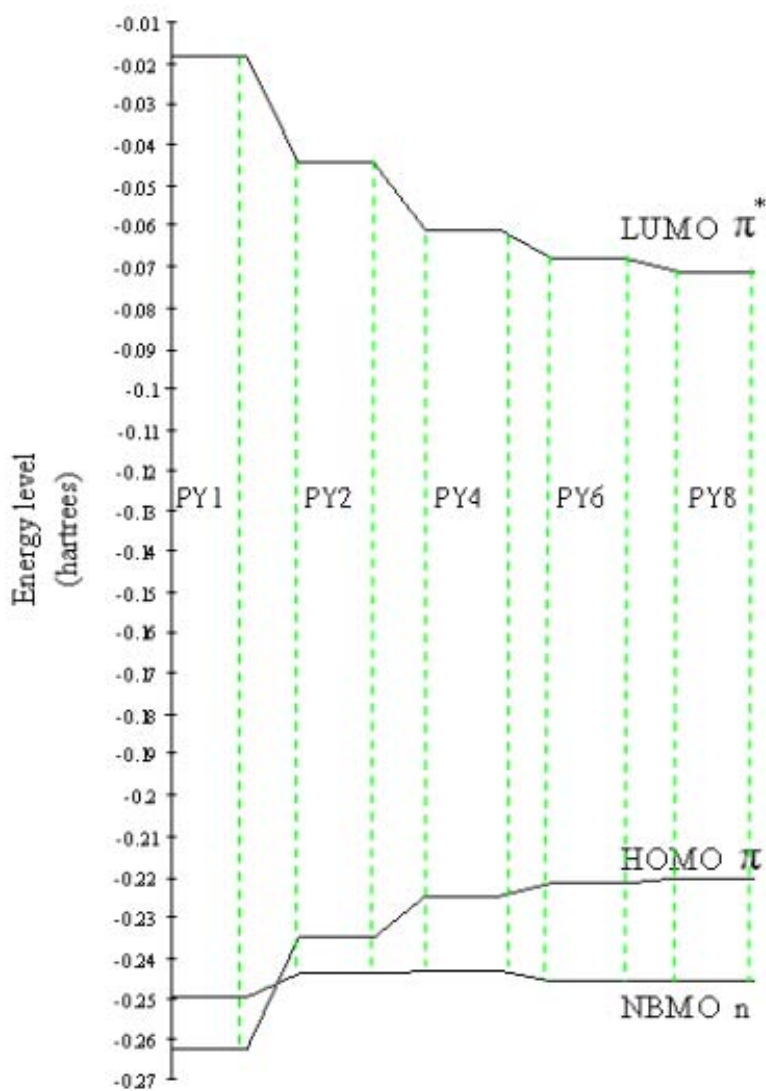


Figure 3.6 Frontier orbital energy levels for pyridine oligomers.

Increased electron density at the pyridine N occurs after protonation. For example, the HOMO ( $n$ ) of a single pyridine has the largest electron density in the N-H<sup>+</sup> bond direction (figure 3.7), so it shifts sharply down to become HOMO-9 after protonation (fig.3.7). On the other hand, HOMO-1 ( $\pi$ ) for this single pyridine does not have any electron density at N, hence it has a smaller downward shift than that of LUMO ( $\pi^*$ ) and the  $\pi$ - $\pi^*$  gap decreases after protonation. Similarly, PY2 also shows the red shift in the  $\pi$ - $\pi^*$  gap after protonation, though the steric repulsion,  $\theta = -126^\circ$ , competes with the coulomb attraction (figure 3.8 and 3.9 and table 3.2).

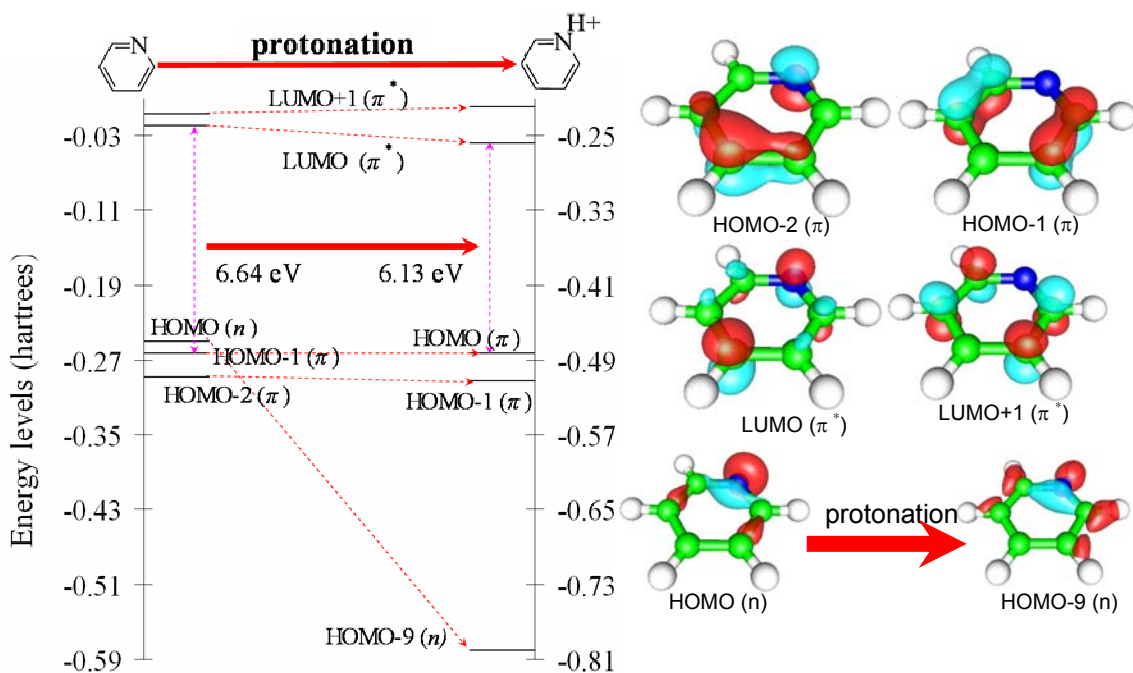


Figure 3.7 Frontier orbital energy levels and electron wavefunctions of pyridine before and after protonation.

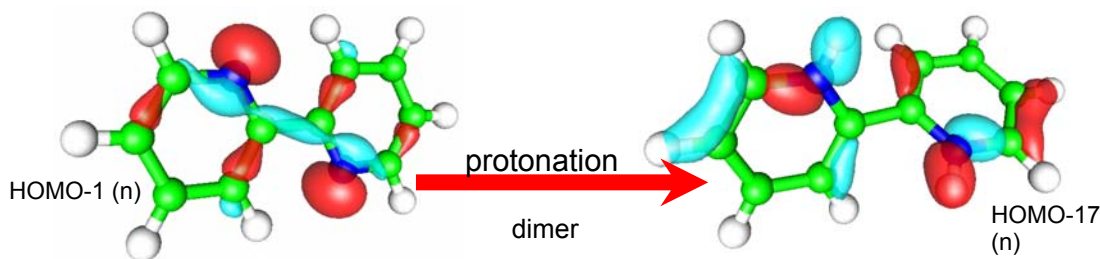


Figure 3.8 Dimer HOMO-1  $n$  (neutral) and HOMO-17  $n$  (protonated).

In order to show the competition between the coulomb attraction and the steric repulsion quantitatively, we decompose the HOMO-1 ( $\pi$ ) and the LUMO ( $\pi^*$ ) energy for single pyridine into three physical terms:

$$\text{Orbital energy } \varepsilon = \langle \text{KE} \rangle + \langle \text{NE} \rangle + \langle \text{EE} \rangle,$$

where KE is kinetic energy, NE is nucleus-electron energy and electron-electron energy. Table 3.1 shows clearly that the change of NE after protonation is dominant for both  $\pi$  and  $\pi^*$  orbitals.

	$\pi$	$\pi^*$
$\Delta\varepsilon$	-5.96 eV	-6.46 eV
$\Delta\text{KE}$	+0.86 eV	+1.00 eV
$\Delta\text{NE}$	-8.09 eV	-10.04 eV
$\Delta\text{EE}$	+1.27 eV	+2.59 eV

Table 3.1 Change of KE, NE and EE for single pyridine due to protonation.

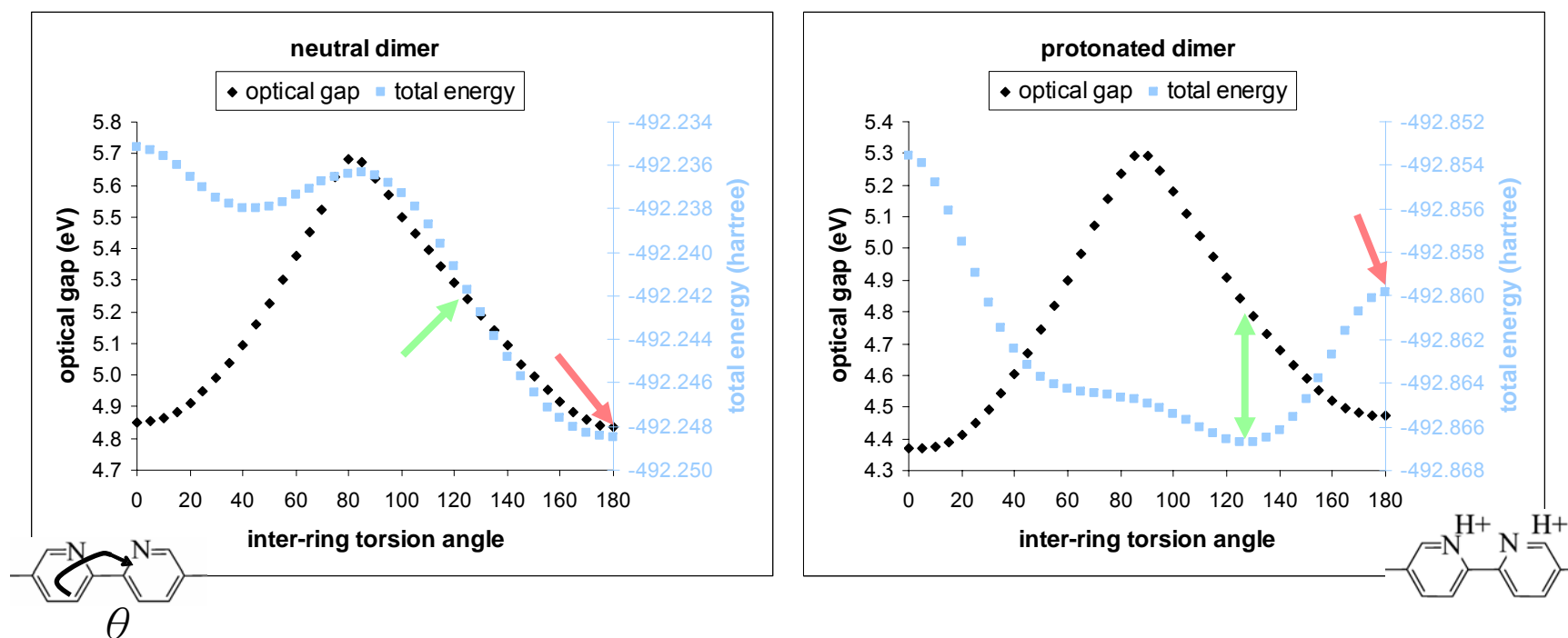


Figure 3.9  $\pi$ - $\pi^*$  gap and total energy for neutral and protonated dimer as a function of  $\theta$ .

Neutral	$\theta = 125^\circ$	$\theta = 180^\circ$
Gap (eV)	5.24	4.83
Energy (hartree)	-492.242	-492.248

Protonated	$\theta = 125^\circ$	$\theta = 180^\circ$
Gap (eV)	4.80	4.47
Energy (hartree)	-492.242	-492.860

Table 3.2  $\pi$ - $\pi^*$  gap and total energy for neutral and protonated dimer at  $125^\circ$  and  $180^\circ$ .

Furthermore, we calculate the increase in the  $\pi\text{-}\pi^*$  gap for a pyridine dimer as the inter-ring torsion angle,  $\theta$ , is increased systematically (figure 3.9). From table 3.2, we can see clearly that after protonation, the lowest energy shifts from  $180^\circ$  to  $125^\circ$  and the  $\pi\text{-}\pi^*$  gap is red shifted for the same angle.

### 3.3 Conclusions

From the previous results of XPS, sulfonic acid containing polymers and molecules do partially protonate pyridine containing polymers. DFT calculations show that the protonation causes the dramatically downward shift in the  $n$  orbital. On the other hand, the coulomb attraction due to protonation of pyridine rings causes red shift in the band gap though the steric repulsion after protonation competes with the attraction. Hence we conclude protonation at polymer-acidic polymer interfaces is responsible for color variation in SCALE devices.

## CHAPTER 4

### TIME OF FLIGHT TECHNIQUE AND ANALYSIS

#### 4.1 Theoretical Background

In a crystal, defects formed by vacancies, dislocations and grain boundaries can scatter charge motions. In disordered organic and polymer semiconducting solids, charges are “trapped” at lower energy sites, and moves through hopping: either phonon-assisted or tunneling. The phonon-carrier interaction is highly field and temperature sensitive. There are several simple models relating mobility with field and temperature.

First, the effective mobility changes in the presence of traps. An example of a simple trap distribution is shown in figure 4.1. Let  $\mu_0$  and  $n_0$  be the mobility and carrier density in the conduction band.  $N_t$  carriers are trapped, with trap depth  $E_t$ . Then the situation can be divided into two cases: shallow traps and deep traps. Let us consider shallow traps first [25], which are characterized by the condition  $t_r \ll t_T$ , with  $t_r$  the lifetime of a carrier in a trap. During the transit, the average mobility is related to the trap-free value by,

$$n_0 \mu_0 = (n_0 + n_t) \mu \quad (4.1)$$

with  $n_t$  the density of trapped charge. At thermal equilibrium, we have,

$$\frac{n_t}{n_c} = \frac{N_t}{N_c} \exp(E_t / kT) \quad (4.2)$$

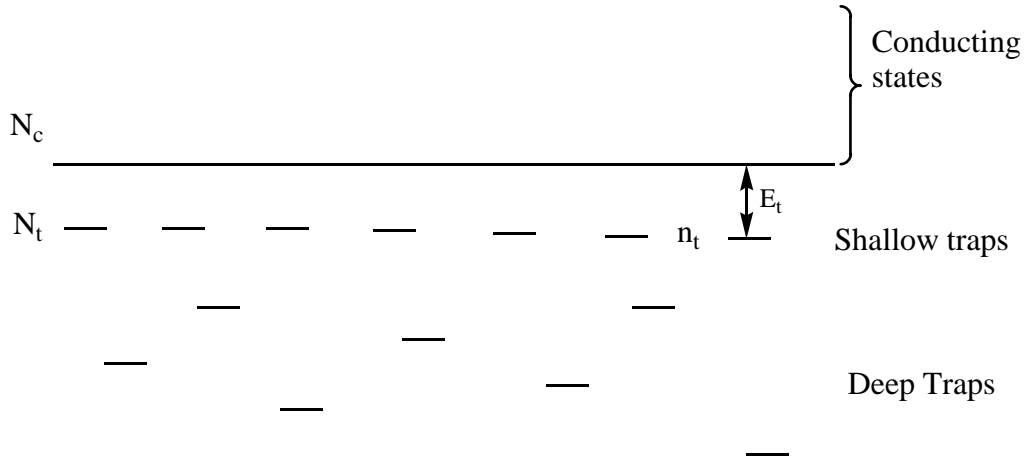


Figure 4.1 Effects of deep and shallow traps.

with  $N_t$  and  $N_c$  the total trap density (at  $E_t$ ) and density of conduction states (at the band edge), respectively. Equations (4.1) and (4.2) lead to the effective mobility,

$$\mu = \mu_0 \left[ 1 + \frac{N_t}{N_c} \exp(E_t / kT) \right]^{-1} \quad (4.3)$$

At sufficiently high temperature,  $\mu \approx \mu_0$ . At low temperatures, the exponential term in (4.3) dominates and,

$$\mu \approx \mu_0 \exp(-E_t / kT) \quad (4.4)$$

The transition between the two types of transport has been observed in experiment [26].

The second group of traps is “deep” trap defined by the condition:  $t_r \gg t_T$ . With the existence of deep traps, some of the carriers will be delayed and we would expect a more complicated dependence of mobility on temperature. If the shallow and deep traps dominate, all the carriers are trapped at least once or even the carriers are transported from trap to trap directly, we encounter the so-called dispersive transport which has been studied for several decades [27, 28, 29].

A simple model for field dependence is the so-called Poole-Frenkel [30, 31] effect, which describes the reduction in ionization energy of a carrier in a coulomb potential by an applied field. The effect of the field is through lowering of the potential barrier as illustrated in figure 4.2 for a one-dimensional case. The electron potential in a field  $E$  is,

$$eEx - \frac{e^2}{4\pi\epsilon_0\epsilon_r|x|} \quad (4.5)$$

By maximizing the potential with  $x > 0$ , one can obtain that the barrier is lowered by  $\beta E^{1/2}$  with  $\beta = 2e^{3/2} / (4\pi\epsilon_0\epsilon_r)^{1/2}$ . And so the effect of field and temperature on conductivity is of the form,

$$\mu(E, T) = \mu_0 \exp(\beta E^{1/2} / k_B T) \quad (4.6)$$

This is sometimes referred as the Poole-Frenkel law [32, 33, 34]. While field dependencies predicted by this relation are frequently observed, experimental values of  $\beta$  are very different from theoretical values.

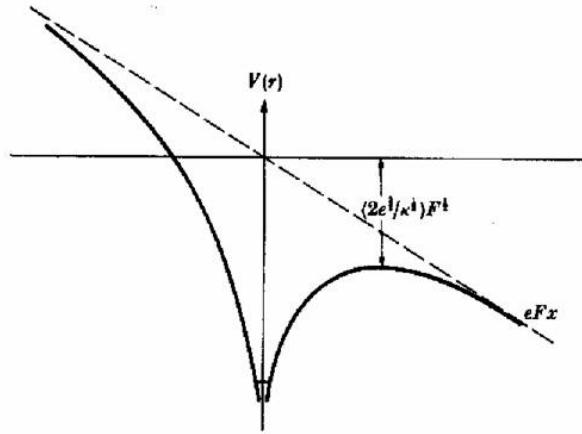


Figure 4.2 Potential energy of an electron under the influence of an electric field  $E$ .

A third model is formalized by Bässler [5]. It considers the distributions of hopping site energies and intersite distances. A fundamental assumption of the Bässler formalism is that upon abandoning long-range order, the transport is through the localized states with energy and intersite distance in Gaussian distribution. It has been shown [5] that a carrier created within a Gaussian density-of-states manifold will relax to mean energy  $\langle \varepsilon \rangle_{\infty} = -\sigma^2 / k_B T$ , with  $\langle \varepsilon \rangle_{\infty}$  the average energy as  $t \rightarrow \infty$ , and  $\sigma$  the standard deviation of the Gaussian distribution. The temperature dependence associated with  $\langle \varepsilon \rangle_{\infty}$  then suggests that the activation energy of low-field mobility must decrease with temperature as,

$$\mu(T) = \mu_0 \exp \left[ - \left( \frac{T_0}{T} \right)^2 \right] \quad (4.7)$$

where  $T_0$  the characteristic temperature proportional to the width of the

distribution. The field dependence of the mobility arises from the fact that a carrier can reach more acceptor or donor sites without thermal activation in the presence of a field than it can in the absence of a field. A first order analysis [35] gives,

$$\mu(T, E) = \mu_0 \exp\left[-\left(\frac{T_0}{T}\right)^2\right] \exp\left(\frac{E}{E_0}\right) \quad (4.8)$$

The important predictions of this model are the field and temperature dependencies of the mobility. The formalism also provides an explanation for a mobility that decreases with increasing field [36]. Results by Schein *et al.* [37] and Hirao *et al.* [38] support Bässler formalism, but studies by Emin [39] and Dunlap [40] have seriously challenged Bässler model.

## 4.2 Experimental Details

TOF was first described by Haynes and Shockley [41] and Lawrence and Gibson [42]. Kepler [43] and LeBlanc [44] first applied TOF to study organic solids, and Vannikov [45] was the first to measure mobilities of polymers by this method. TOF was mainly used to study transport properties of high mobility inorganic solids at early times. As interest grew in the applications of polymers to xerography in 1970s and of organic and polymers in OLED and FET devices in 1990s, TOF are more often employed to measure the mobilities of semiconducting organic and polymers [46, 47, 48]. During the past several

decades, TOF measurements have become the conventional method for studies of transport phenomena in organic and polymers.

The schematic diagram of TOF is illustrated in figure 4.3. A sample with thickness  $d$  is sandwiched between two planar metal electrodes. The top electrode is

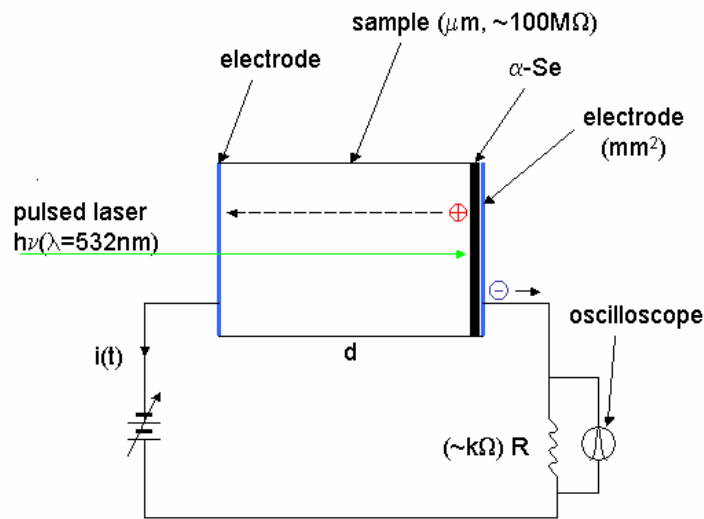


Figure 4.3 A typical experiment setup for measuring mobility using TOF.

semitransparent and should be a non-injecting or blocking electrode for the carrier transported across the sample. The two electrodes are connected to an external circuit via a resistor with resistance  $R$  and a battery with potential  $V$ . The carriers are then generated with a short flash of laser pulse absorbed in a thickness  $\delta$ , with  $\delta \ll d$ . The light pulse duration  $t_e$  should be short, i.e.,  $t_e \ll t_T$ , with  $t_T$  the transit time. The light exposure creates bound electron-hole pairs near one of the electrodes. Under the influence of the applied electric field, a

fraction of the pairs separate and then drift in a sheet across the sample, inducing a time dependent photocurrent in the external circuit. The transient photocurrent is recorded with a high-resolution digital oscilloscope. By switching the polarity of the battery, one can measure either hole or electron photocurrent.

The first condition for TOF is that the amount of charge generated should be small enough so that space-charge effects do not change the internal field strength significantly. This will be true as long as the injected charge  $q_0$  satisfies,

$$q_0 \ll CV \quad (4.9)$$

with  $C$  the sample capacitance. The shape of the leading edge of the drifting current can broaden as a result of the mutual repulsion of the carriers within the generation volume. It has been shown [49] that the error in transit time due to this mutual repulsion is  $\Delta t/t_T \approx q_0/CV$ . But on the other hand,  $q_0$  should be large enough to give unequivocal signals.

The second condition for conventional TOF is that the circuit reaction time  $\tau = RC$  is much smaller compared with the average drifting time of the charges. A small value of  $\tau$  can be realized by choosing small  $R$  or  $C$ . But  $R$  has some lower bound so that the oscilloscope has enough precision. As capacitance is proportional to sample area and inversely proportional to sample thickness, small  $C$  can be realized with higher thickness and smaller cross section.

A third condition requires that the dielectric relaxation time  $\tau_0 = \rho\epsilon\epsilon_0$  be long compared to the transit time, with  $\rho$  the dark resistivity. This is the time required for the insulator to restore itself to the state of neutrality after a small

change in the carrier population. The intrinsic concentration of carriers is very small for materials with small dielectric relaxation time [49]. Organic and polymeric solids have dark resistivities such that this condition for TOF is readily satisfied in most materials of potential interest for xerography, field effect transistor and LEDs.

In TOF measurements, charge injection can be accomplished by direct photoexcitation or by a photoemitting electrode. While direct photoexcitation is a simpler technique, it has two fundamental limitations. First, the technique is limited to photoconductors. Second, the TOF technique is usually based on the assumption that the charge is injected at one surface. This requires that the light for exposures be very strongly absorbed near an electrode. For these reasons, charge injection from a photoemitting electrode has become a standard technique. The more common electrodes are  $\alpha$ -Se,  $\alpha$ -As<sub>2</sub>Se<sub>3</sub>, or the phthalocyanines. In our experiments we evaporate a thin layer of  $\alpha$ -Se between the semitransparent electrode and sample as a photoemitting electrode. A characteristic of this type of photocurrent is that it does not show a plateau region but increases continuously with time and then decreases sharply. It has been claimed [50] that this phenomena is due to delayed charge injection, i.e. all charges are trapped before they started to drift.

During the past several decades, Time-Of-Flight photocurrent measurements have become the conventional method for studies of transport phenomena in doped polymers. The fundamental limitation is that it is difficult to

measure mobilities in the presence of trapping.

#### 4.2.1 Materials Preparation

The semitransparent electrode in our experiment is ITO (Indium-Tin Oxide), a layer pre-deposited on a glass substrate. The sample with thickness from several hundred nanometers to several microns is then deposited by heat evaporation (for materials with small organic molecules) or coated by spin coating (for polymers). A thin layer (10~30nm) of  $\alpha$ -Se is deposited by vacuum deposition before or after sample deposition, depending on the desired configuration. Finally, a metal (usually Al) is deposited as the second electrode by vacuum evaporation. The device has a configuration as ITO/Se/Sample/Al or ITO/Sample/Se/Al. The thickness of the sample is measured with an Alpha-Step 500 Surface Profiler. Figure 4.4 is an example using Alpha-step to measure sample thickness.

Sample evaporation is accomplished in a chamber with low vacuum ( $<10^{-5}$  torr , by diffusion pump). The roughness and thickness of the sample can be controlled by evaporation rate and time. The thickness of the sample can be read on a crystal monitor calibrated with the Alpha-step profiler.

For spin coating, one first dissolves the material into some organic solvent, and then spin coats the solution on the ITO glass, a film is then formed after the solvent is evaporated, and finally the film is dried in a

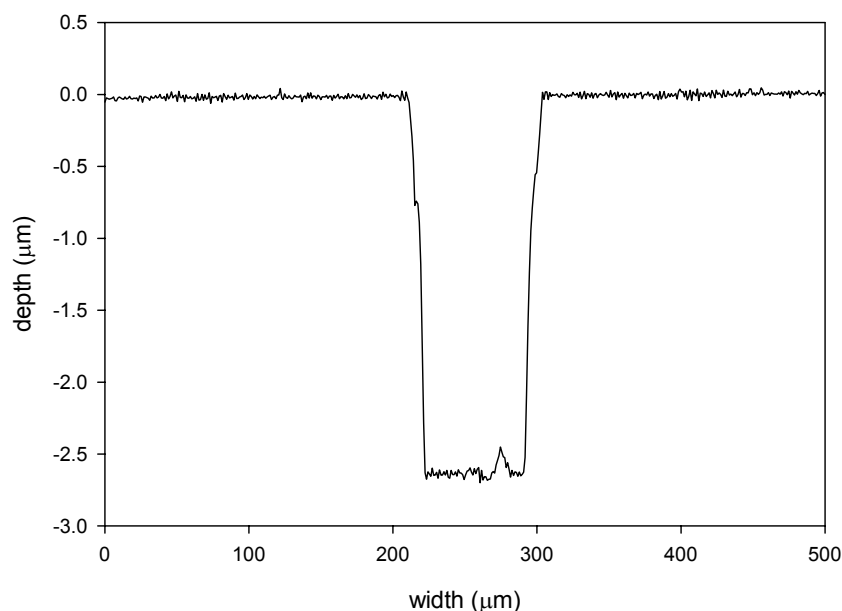


Figure 4.4 Profiler thickness measurement.

Upper level is the surface of sample, and lower level corresponds to substrate surface. The difference ( $\sim 2.56\mu\text{m}$ ) is the thickness of the sample.

vacuum oven at temperature  $50\text{-}80\text{ }^{\circ}\text{C}$  for 2-3 hours. The thickness of the sample film is controlled by choosing the spinning speed (usually several thousand rpm) and the solution concentration (several tens mg/ml). One disadvantage of spin coating is that the film is not uniform, because it is difficult to totally remove the solvent from the film. Another disadvantage is that it is very difficult to make films thicker than a micron, and the quality of film becomes worse as it gets thicker. Because polymer solids are not possible to be evaporated, spin coating is usually the best choice.

#### 4.2.2 Experimental Setup

The sample is connected through the configuration as described in figure 4.3. Then a pulsed laser is turned on to produce charges in the thin Se layer. Under the electric field supplied by the battery, one sign of charges drifts to the other electrode, and the other sign of charges moves through the circuit. A digital oscilloscope is used to measure the voltage change of the resistor in the circuit. In our experiment, we use a Continuum Surelite I pulsed laser. We use the wavelength 532 nm so that absorption is occurred only in Se layer. The materials investigated in this study (Chapter 5) do not have substantial photo absorption at this wavelength [51], but  $\alpha$ -Se does [52]. The pulse duration is about 10ns, much shorter than the charge drifting times ( $\mu$ s). And the pulse frequency is 15 Hz such that the second pulse will not disturb the charges produced by the first pulse. The power of the laser is several milliwatts. But for some strong absorption materials we use glass filters to decrease the power to microwatts to control the amount of charges produced by the laser.

The electric field is adjusted through the battery in figure 4.3. We have used HP 6218A power supply to replace the battery, with range from zero to 50 volts. If higher voltage is needed, we use several power supplies in series. Because there is uncertainty of the work function difference between the two electrodes (for ITO and Al, it's about 0.3-0.5V), we do not use battery voltage lower than 10V.

The resistance of the resistor has to be in the proper range. Small resistance will decrease the signal-noise ratio of the oscilloscope, whereas large resistance will share the voltage with the sample. The resistance in our experiment is chosen to be 10-20k $\Omega$ . The voltage of the resistor produced by the photocurrent is measured with a Tektronix TDS 430A Digital Oscilloscope with frequency 400MHz.

Finally, the signal recorded by the oscilloscope is analyzed by the models, which are described in section 4.3 and 4.4, to obtain information about the charge transport in the sample.

### 4.3 Scher-Montroll Model

In an ideal case when all the charges propagate in a plane wave, the photocurrent pulse should display a rectangle-like shape when the circuit reaction time is negligible, as illustrated in figure 4.5a.

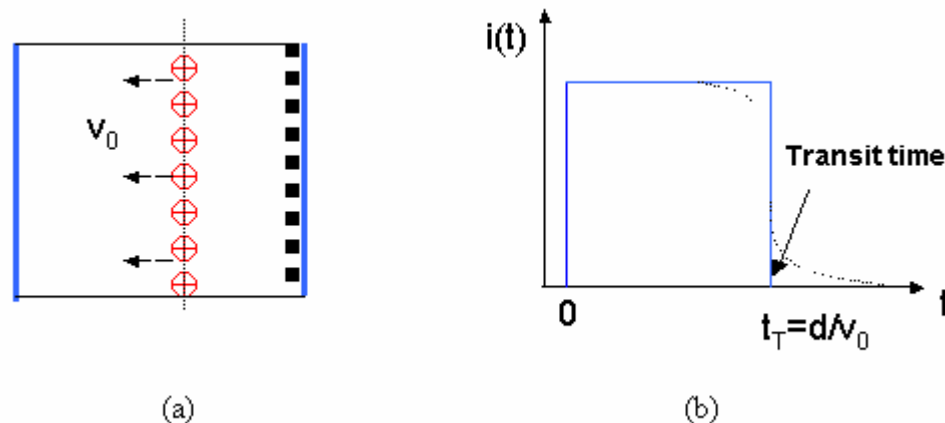


Figure 4.5 Ideal case when charges drift in a plane wave.  
 (a) The measured photocurrent has a rectangle-like shape.  
 (b) The tail in is due to circuit reaction dela.

Ideally, there is a sharp decrease at the time when the carriers exit the sample. The time corresponding to this decrease is usually defined as the transit time. A small tail decaying exponentially should exist if the circuit reaction time is not zero. Figure 4.5b is the measured photocurrent of a real material [53]. In addition to the plateau, the photocurrent in this figure displays a sharp decrease near the origin, and fatter tail than the ideal case. Although the sharp decrease near the origin has been observed in many experiments [46, 47, 48], a reasonable explanation has not been proposed yet. The fact that the measured tail is longer than an exponential decay can be explained by the existence of traps. Traps are some localized states for electrons or holes. When the trap density is not high, the majority of the charges will drift in a thin plane.

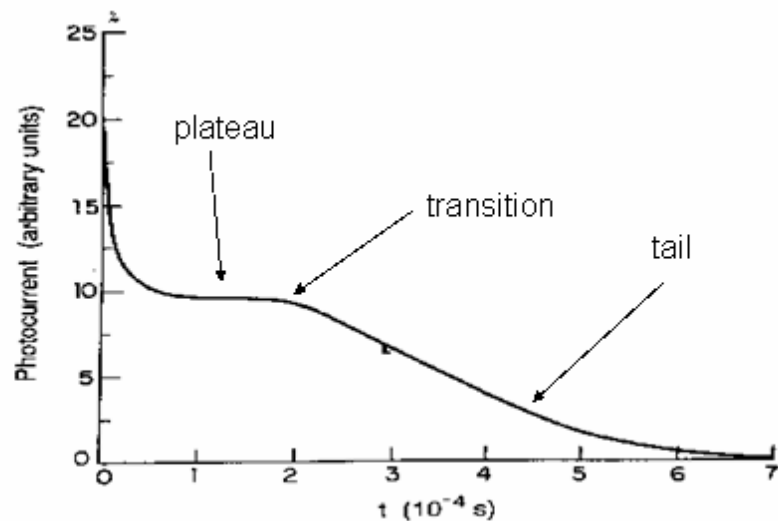


Figure 4.6 A typical photocurrent transient.

The transit time is at the intersection of plateau and tailing edge of the photocurrent.

An explanation in terms of density-of states is illustrated in figure.4.7 [54]. In a perfect crystal, the free electron states form bands separated by gaps with sharply defined edges, as shown in figure 4.7a [54]. In the presence of a single localized imperfection, the band edges will not be disturbed if there is no interaction between the impurity state and the crystal. Then a carrier will move essentially as if it were in a perfect crystal. The impurity level will be sharp, as shown in figure 4.7b. But if the impurity or defect level does interact with the lattice, then the energy levels of the impurity and the crystal will be changed. As shown in figure 4.7c, the interaction between the impurity level and valence or conduction bands forms a band of localized states. A carrier moving in the crystal can be trapped or scattered by these localized states, exhibiting a transient photocurrent shape as shown in figure 4.8 [55].

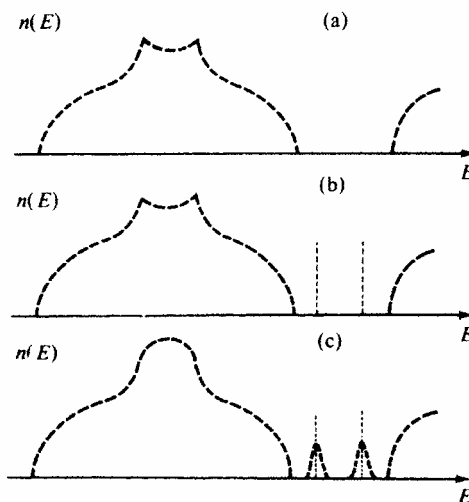


Figure 4.7 Density of electronic states  $n(E)$  as a function of energy  $E$ .

- (a) a perfect crystal
- (b) a crystal containing only one localized imperfection
- (c) a crystal containing a low concentration of localized imperfection

In the presence of translational or compositional disorders, the localized states in the gap can trail off in a continuous tail from the valence and conduction bands. The states are so numerous that transport is possible from one defect site to another. Since the motion of the carrier is wavelike in the extended states forming the conduction band, and is that of phonon-assisted hopping in the localized states, the mobility displays a gap [25].

In the case of amorphous materials or of materials with an almost continuous distribution of trapping centers extending deep into the forbidden gap, the shape of the transient photocurrent will resemble that shown in figure 4.8 [55]. There is a sharp spike followed by a rapid decay to a plateau that tails off gradually so that it is difficult, sometimes impossible to determine the transit time. This type of transport is referred as dispersive transport, which is characteristic of most amorphous inorganic solids and organic and polymeric solids.

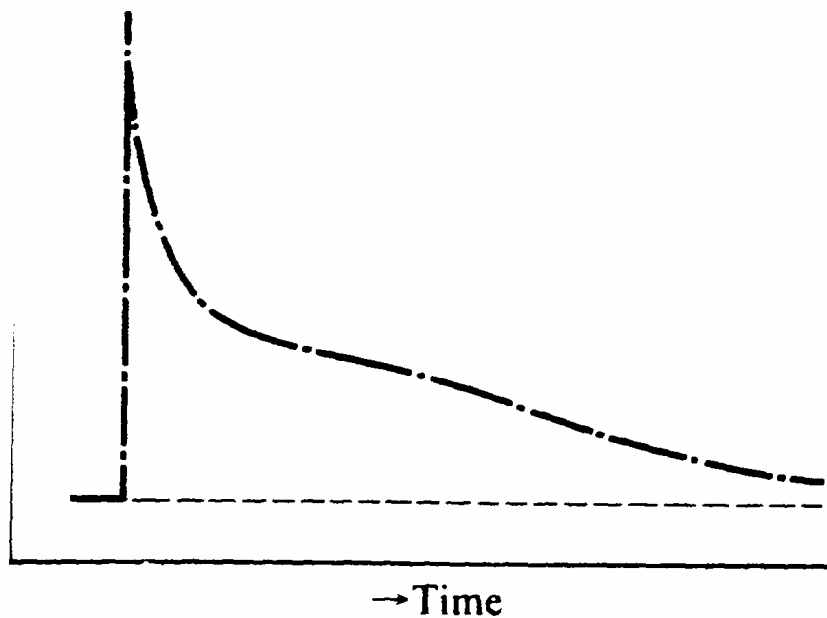


Figure 4.8 Photocurrent broadened by traps.

In 1975, Scher and Montroll [56] developed a statistical theory to study the mobility in dispersive transport with disorder. The Scher-Montroll model has been widely used to describe dispersive phenomena in amorphous solids and doped polymer systems.

Their model system consists of a random array of hopping sites within a regular lattice of cells made up of these sites (figure 4.9). The waiting time for a particle on a given site follows a Continuous Time Random Walk (CTRW) Model. In the absence of disorder, the transition rate between hopping sites is a constant, and thus both the dwell time and hopping time obey an exponential distribution. But the presence of disorder changes the transition rate into a random variable, and as an effect the TOF photocurrent displays a long tail. Scher and Montroll proposed a power distribution for waiting time to describe the effect of disorder,

$$\psi(t) \sim t^{-(1+\alpha)} \quad (4.10)$$

where  $\alpha$  a disorder parameter that has values between zero and unity.

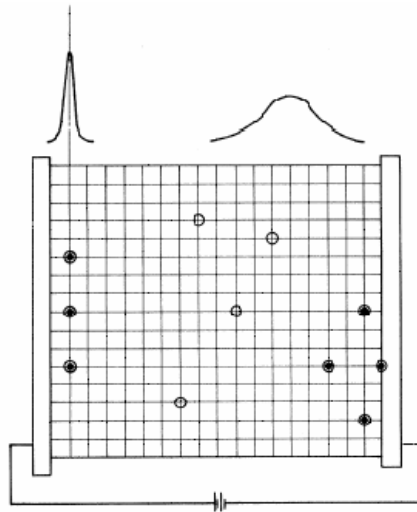


Figure 4.9 Schematic diagram for random walk model. The carriers are injected as from the left side and propagate toward an absorbing barrier on the right side.

The more disordered the material, the smaller the value of  $\alpha$  and the more dispersive the transport. One way to look at this distribution function is that in  $\psi(t)$  decreases with increasing time. Thus, at shorter times there is a greater fractional change than at longer times.

A key prediction by Scher-Montroll model is that the transient photocurrent will decay as,

$$i(t) \sim \begin{cases} t^{-(1-\alpha)}, \dots, t < t_T \\ t^{-(1+\alpha)}, \dots, t > t_T \end{cases} \quad (4.11)$$

This relation is sometimes called “power law”, in which the tail current obeys the power relation. Following this relation, one can easily obtain the transit time by plotting the current and time in log-log scale. The point of intersection of the two branches in (4.11) defines the transit time. According to this model, the transit time is,

$$t_T \sim \frac{C}{W_0} \left| \frac{L}{l(E)} \right|^{1/\alpha} \exp\left(\frac{\Delta_0}{kT}\right) \quad (4.12)$$

where  $C$  is a constant of order unit,  $W_0$  a scaling factor,  $\Delta_0$  a zero field activation energy, and  $l(E)$  the mean displacement in the field direction per hop. At low field, it may be assumed that  $l(E) \propto E$  [32], thus the transit time varies with thickness and field as  $(L/E)^{1/\alpha}$ . Figure 4.10 [57] shows a successful application of Scher-Montroll model to study the mobility in dispersive transport [58].

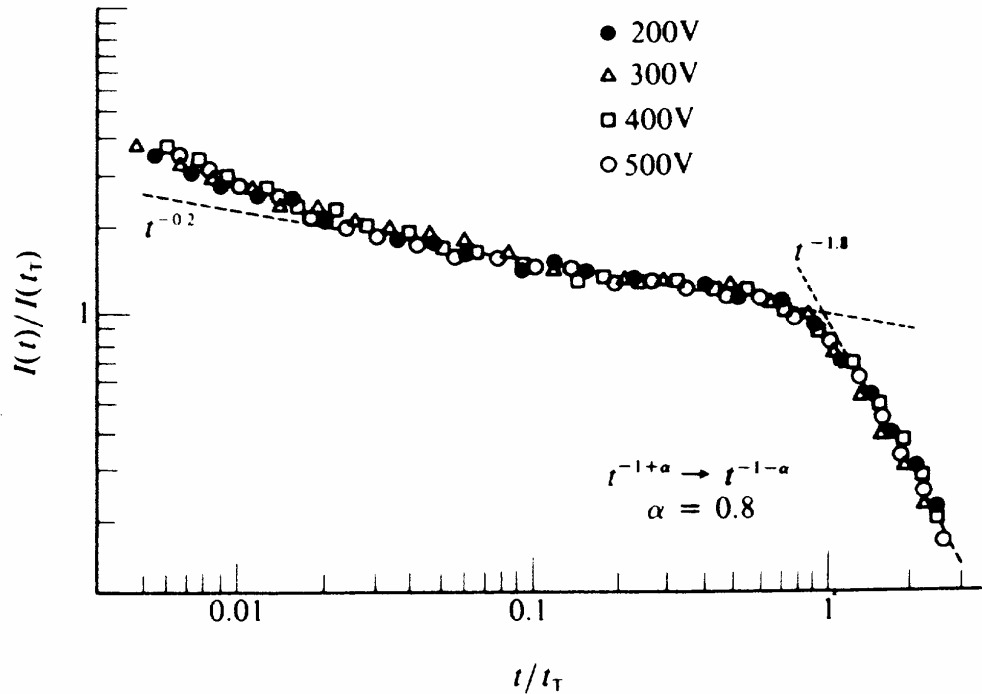


Figure 4.10 A  $\log(I/I_T) - \log(t/t_T)$  plot for 1:1 TNF-PVK.  
The slopes of the Dashed lines are  $-0.2$  and  $-1.8$ .

The most important assumption in Scher-Montroll model is the power waiting time distribution (4.10), which is the reason for its success in amorphous inorganic solids, but which is also the cause of its failure in a lot of materials especially dispersive organic and polymeric solids. Bässler [59] has argued that the waiting time distribution  $\psi(t) \sim t^{-(1+\alpha)}$  in Scher and Montroll's model is realized in materials in which multiple trapping within an exponential distribution prevails, but organic glasses and molecularly doped polymers do not fall into this category. In most cases, the charge distribution can be well approximated by a Gaussian, which is not consistent with Scher-Montroll model. Furthermore, Godson and Hirsch [60] early observed that in 1:1 TNF.PVK, the tail of the photocurrent was

closer to an exponential than a power law, and we have observed the same phenomena in our studying organic and polymeric semiconducting solids.

Even for those materials that satisfy the assumptions in Scher-Montroll model, we may still encounter practical difficulty. In order to apply Scher-Montroll's power relation, one requires that the circuit reaction time  $\tau = RC$  be much smaller than the transit time  $t_T$  so that the measured photocurrent is the same as the drifting current in the sample. Another requirement is that the quantity of charge produced by the laser is much less than the product of the sample capacitance and battery voltage (4.9), so that the drifting charges perturb the external electric field as less as possible. But at the same time the quantity of charge should be large enough to give unequivocal signals. However, in many low mobility organic and polymeric materials, these conditions are sometimes difficult to be satisfied simultaneously, a case which has limited the applicability of Scher-Montroll's method in these materials. A lot of efforts have been applied to solve this problem, but so far, it has not been successfully solved [61].

As we have discussed, the effect of traps is that the charges do not drift uniformly, not even the majority of charges do. Scher-Montroll model [56] and other studies [61] give results that the transit time for dispersive transport is a function of sample thickness. As a result, an interpretation in terms of charge carrier mobility is not meaningful. Scott et al. [62] have described a method to obtain the mean carrier mobility defined by a carrier velocity distribution. In the framework of Scher-Montroll model, they found that the velocity distribution can

be described by a Gaussian function. Then the mean mobility is the average of the mobilities of all the carriers. They applied this model to diethylaminobenzaldehyde-methylphenyl hydrazone (DEMPH) doped into polycarbonate (PC) at a concentration of 50% obtaining a good fit and a mobility in the order of  $10^{-5} \text{ cm}^2 / \text{Vs}$ .

#### 4.4 A Proposed Model to Fit TOF Photocurrent

In 2002, Xiaoming Zou proposed a stochastic model to simulate TOF photocurrent. For detailed explanations, please refer to his dissertation [63]. Let me briefly introduce his model in this section.

The model is based on a simple assumption that the sample can be well approximated as a capacitor with capacitance  $C$ . The capacitor is symmetric and uniform so that it is treated as one dimension in his model. A schematic diagram of his deduction is shown in figure 4.11. Suppose that a single short laser pulse (the width of pulse is negligible) produces many electron-hole pairs or excitons in the Selenium layer, and then the external electric field by the battery successfully separates a total amount of positive charge  $q_0$  and an equal amount of negative charge. The negative charge then drifts across the sample to the other side, while the positive charge flows to the other side through the external circuit. The charges inside the sample follow a random walk with different hopping probabilities in forward and backward directions [64].

When there is no trap in the sample, macroscopically all the negative charges will drift to the other side in a plane and the charge density is a delta function. If traps exist, the charges will be trapped and repeatedly released many times during their drift.  $\rho(x,t)$  is used to describe the line charge density for those charges drifting in the sample at position  $x$  and time  $t$ . His model assumes this function is continuous and differentiable.

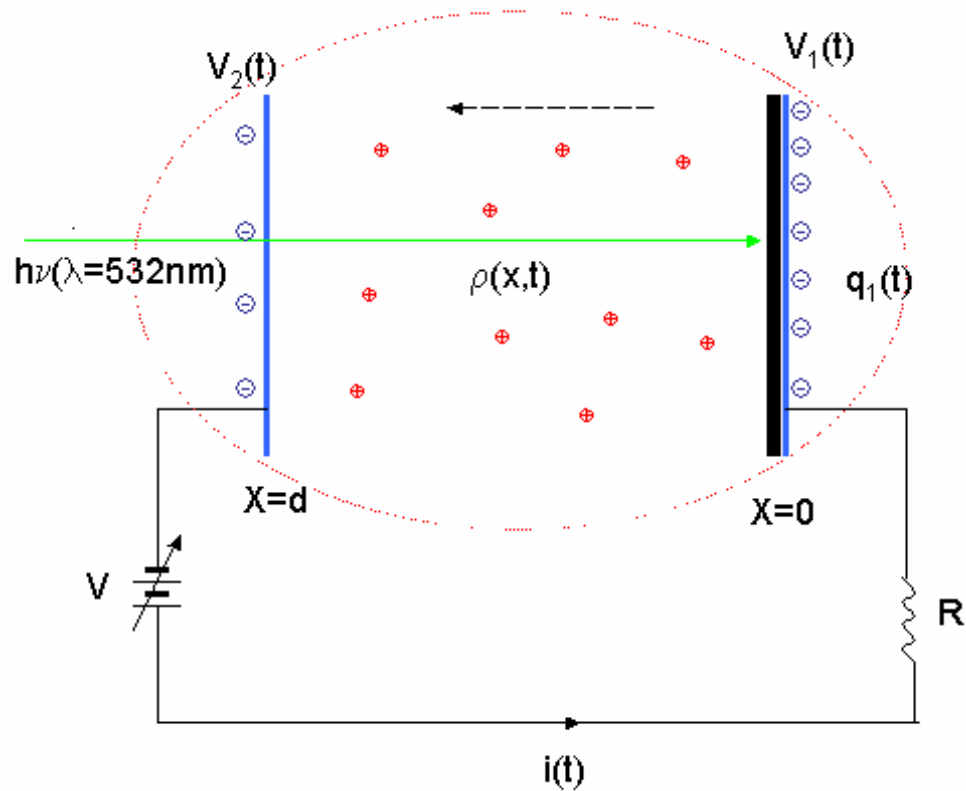


Figure 4.11 Schematic diagram for the line charge density  $\rho(x,t)$ .

On the basis of all these macroscopic assumptions, Zou has derived a differential equation describing the dynamic behavior of photocurrent in TOF.

$$\tau \frac{d}{dt} i(t) = -i(t) + \bar{i}_{in}(t)$$

where,

$$\bar{i}_{in}(t) = \frac{1}{d} \int_0^d i_{in}(x,t) dx$$

$$i_{in}(x,t) = \frac{\partial}{\partial t} \int_0^x \rho(z,t) dz$$

with  $\bar{i}_{in}(t)$  the average drifting current,  $i_{in}(x,t)$  the drifting current at position  $x$  and time  $t$  inside the sample, and  $\tau = RC$  which is the circuit characteristic constant.

The differential equation has a general solution  $i(t) = e^{-t/\tau} \left[ \int_0^t \bar{i}_{in}(t') e^{t'/\tau} dt' / \tau \right]$ . The solution depends on the average drifting current, which depends on the charge density function. Furthermore, after neglecting some unimportant terms, one can obtain an expression for the photocurrent as,

$$i(t) = \frac{q_0}{d} e^{-t/\tau} \left[ \int_0^t e^{t'/\tau} \left[ \int_0^{d/t'} v f_v(v,t) dv \right] dt' / \tau \right]$$

where,  $f_v(v,t)$  is the charge velocity distribution, i.e.,

$$q(x,t) = q_0 \int_0^{x/t} f_v(v,t) dv$$

Finally, If the distance between the location, where charges are photo-induced, and the electrode is much smaller than the thickness of the sample, then the velocity distribution can be well approximated as Gaussian function,

$$f_v(v,t) = \frac{1}{\sqrt{2\pi\sigma_0^2/t}} e^{-\frac{(v-v_0)^2}{2\sigma_0^2/t}},$$

where  $\sigma_0^2/t$  is the variance and  $v_0$  is the mean.

By fitting the simulated photocurrent to the experimental one, four parameters,  $\tau, \sigma_0, v_0$  and  $q_0$  could be obtained. The Gaussian distribution for drifting velocity in TOF has also been observed and used in other studies [65, 66, 67]. After obtaining these values from fitting, we can find the average velocity by the following expression,

$$\langle v \rangle = \frac{\int_0^\infty dt \int_0^\infty v f_v(v, t) dv}{\int_0^\infty dt \int_0^\infty f_v(v, t) dv},$$

and the average mobility can be found by

$$\langle \mu \rangle = \langle v \rangle / E.$$

The mobilities of some organic molecules and polymers obtained by Zou's model were reported in good agreement with the values obtained by other models [63].

## CHAPTER 5

### TIME OF FLIGHT MEASUREMENT FOR NEW MATERIALS

Two new materials investigated in this thesis for their mobilities by TOF are Tris-[4-(2-{4-[3,6-Bis(4-t-butylphenyl)cabazole-9-yl]phenyl}vinyl)phenyl]amine (TPA-Cz3d) and 9,10-Bis(2-{4-[5-(4-dodecyloxyphenyl)-1,3,4-oxadiazole-2-yl]phenyl}ethynyl) anthracene (ANTH-OXA6t-OC12). Their chemical structures are shown in figure 5.1 and figure 5.2 respectively.

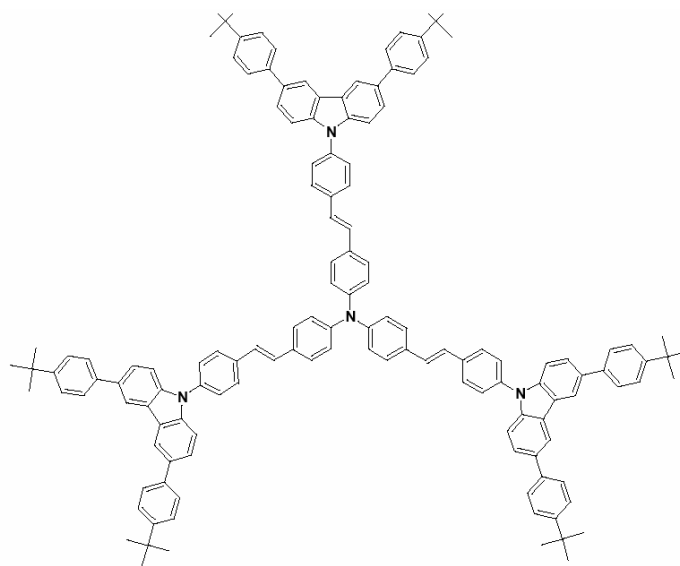


Figure 5.1 Chemical structure of TPA-Cz3d.

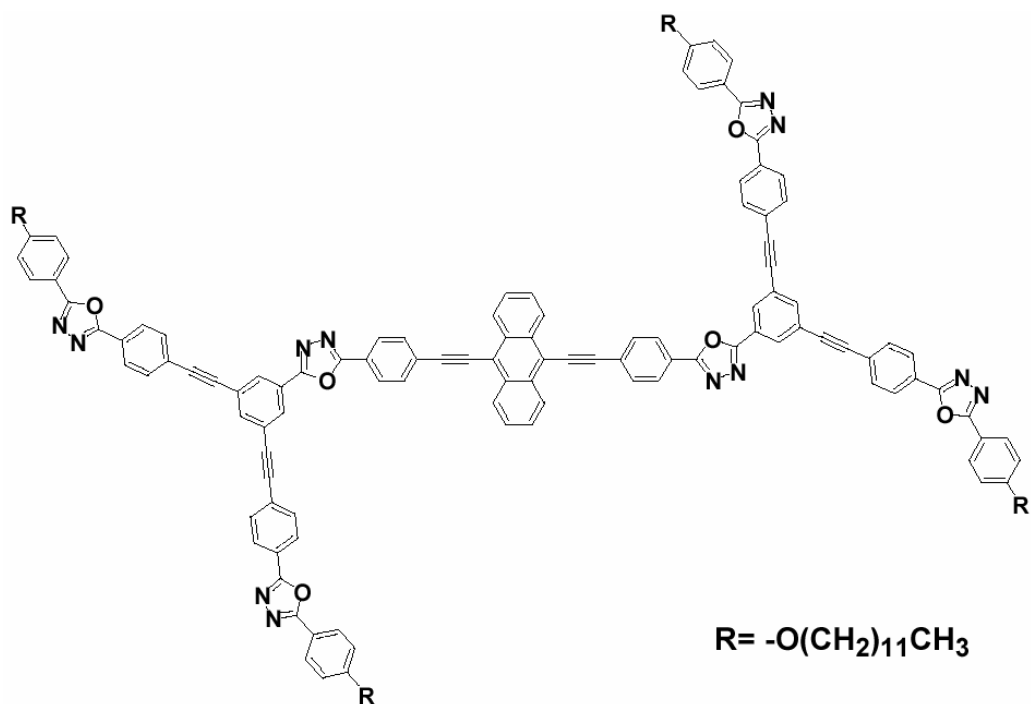


Figure 5.2 Chemical structure of ANTH-OXA6t-OC12.

These two materials were synthesized by Soon-Wook Cha [51]. Cha also has reported their absorption spectra in his PhD dissertation [51].

Although the mobilities were first time ever measured, the results reported in this work are only at the preliminary level. In order to publish the results, further measurements and analyses are required. Both Zou's model and Scher-Montroll (S-M) model are employed to find the mobilities.

### 5.1 TPA-Cz3d

The hole mobilities for device ITO/Se(30nm)/TPA-Cz3d (0.71 $\mu$ m)/Al(100nm), which are obtained by Zou's model and S-M model under different applied voltages at room temperature ( $\sim$ 300K), are given below.

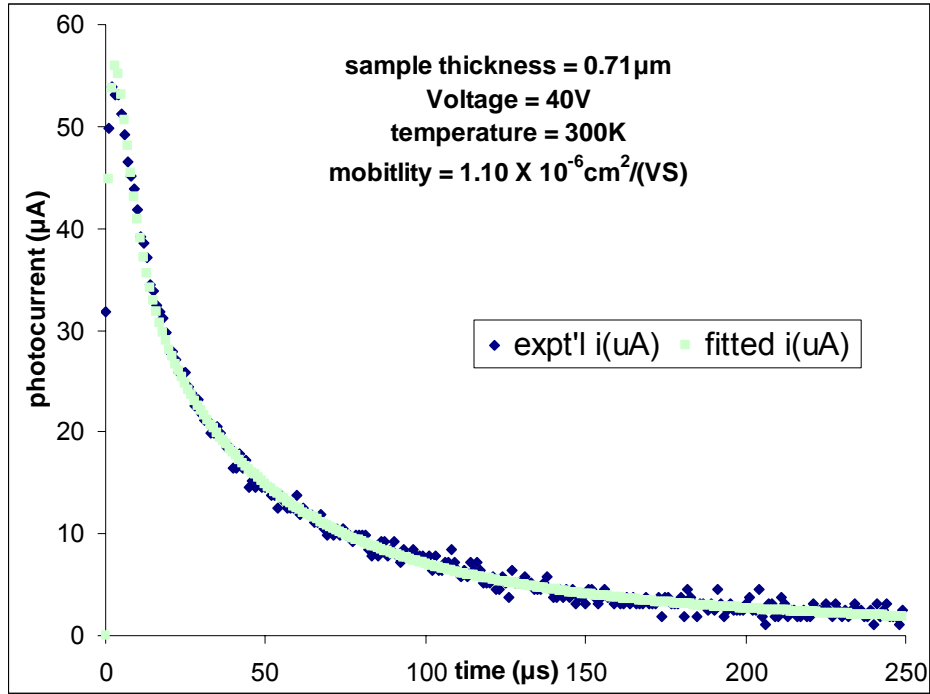


Figure 5.3 TPA-Cz3d: Experimental and fitted photocurrent for 40V.

$$\tau = 3.17 \mu s, \sigma_0 = 0.0549 m/s, v_0 = 0.00268 m/s, q_0 = 2931 pC.$$

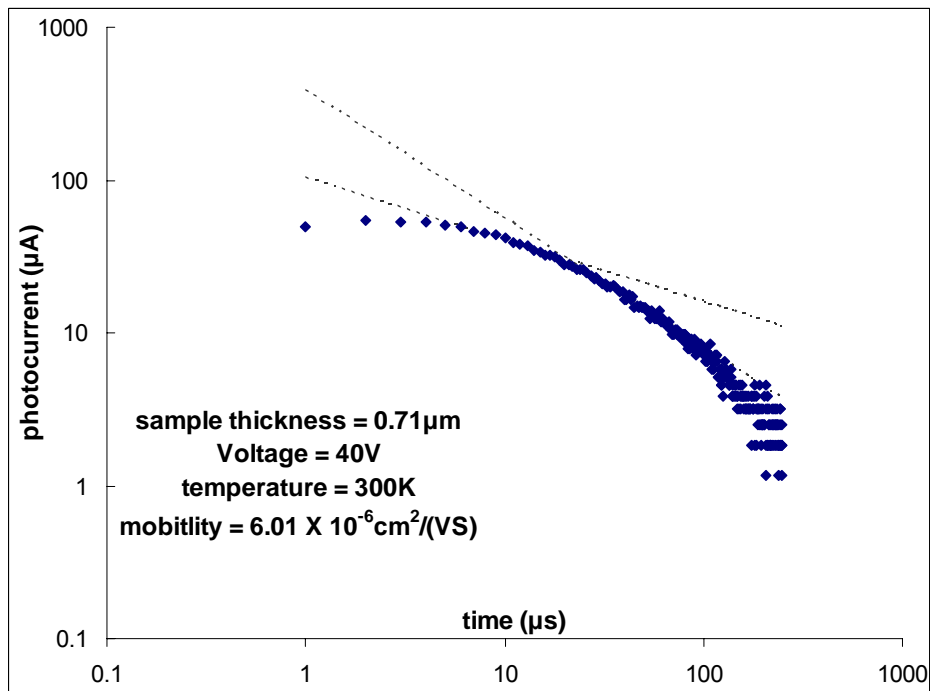


Figure 5.4 TPA-Cz3d: Log-Log plot of the photocurrent for 40V.

$$\alpha_{initial} = 0.60, \alpha_{final} = -0.16 \text{ and the transit time (intersection) is at } 20.96 \mu s.$$

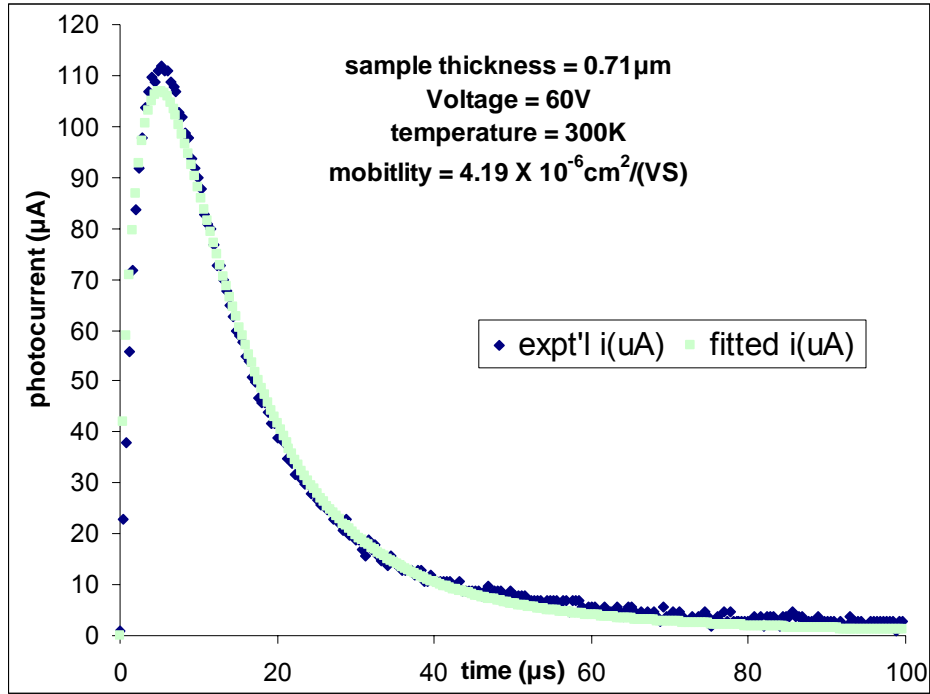


Figure 5.5 TPA-Cz3d: Experimental and fitted photocurrent for 60V.

$$\tau = 5.93\mu s, \sigma_0 = 0.159m/s, v_0 = 0.0250m/s, q_0 = 2303pC$$

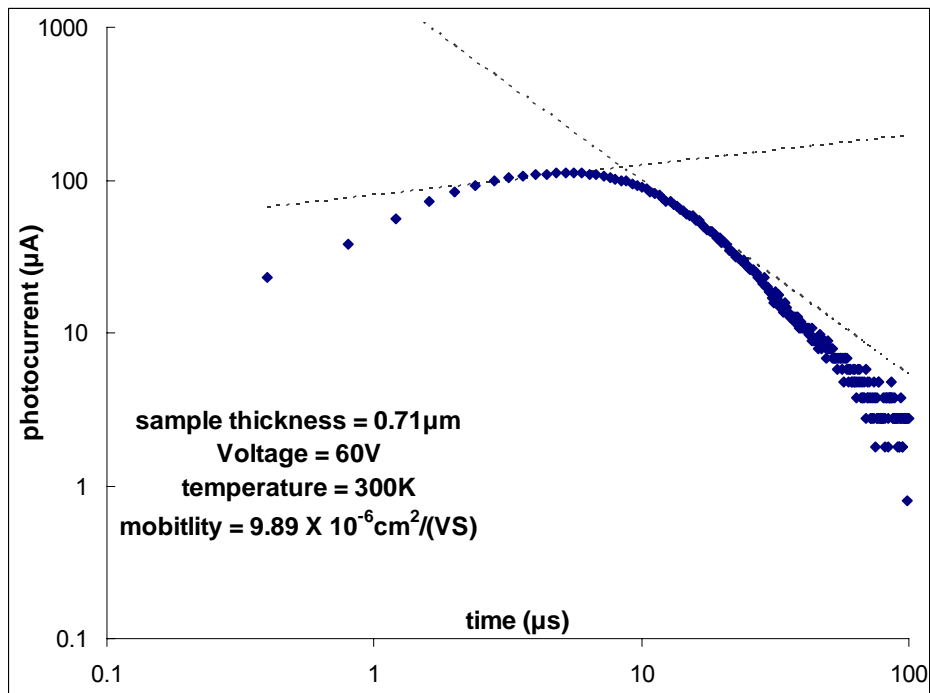


Figure 5.6 TPA-Cz3d: Log-Log plot of the photocurrent for 60V.

$$\alpha_{initial} = 1.20, \alpha_{final} = 0.27 \text{ and the transit time (intersection) is at } 8.50\mu s.$$

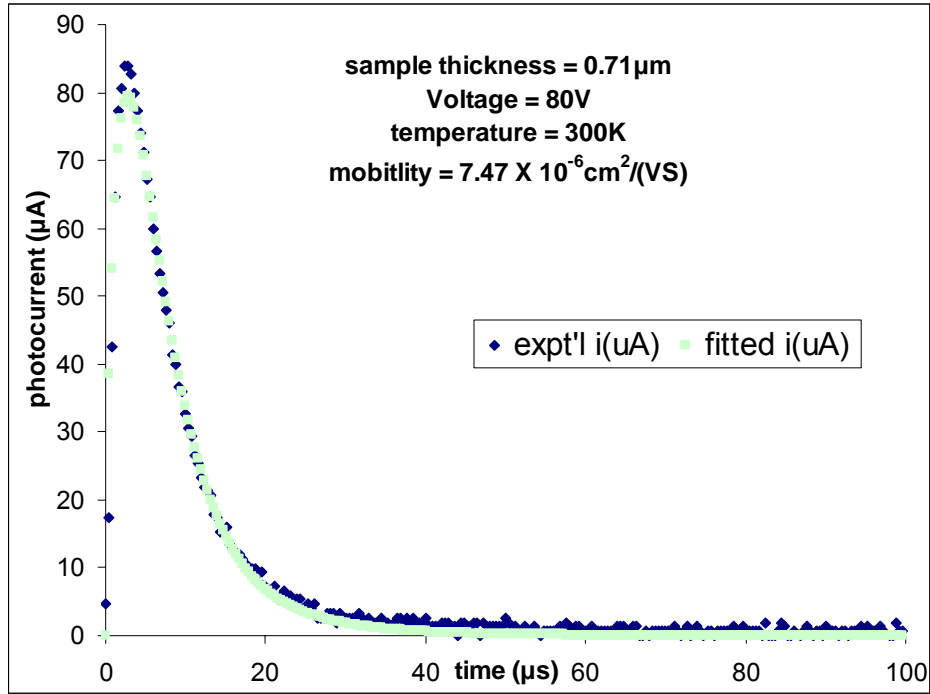


Figure 5.7 TPA-Cz3d: Experimental and fitted photocurrent for 80V.

$$\tau = 3.53 \mu s, \sigma_0 = 0.227 m/s, v_0 = 0.0778 m/s, q_0 = 835 pC$$

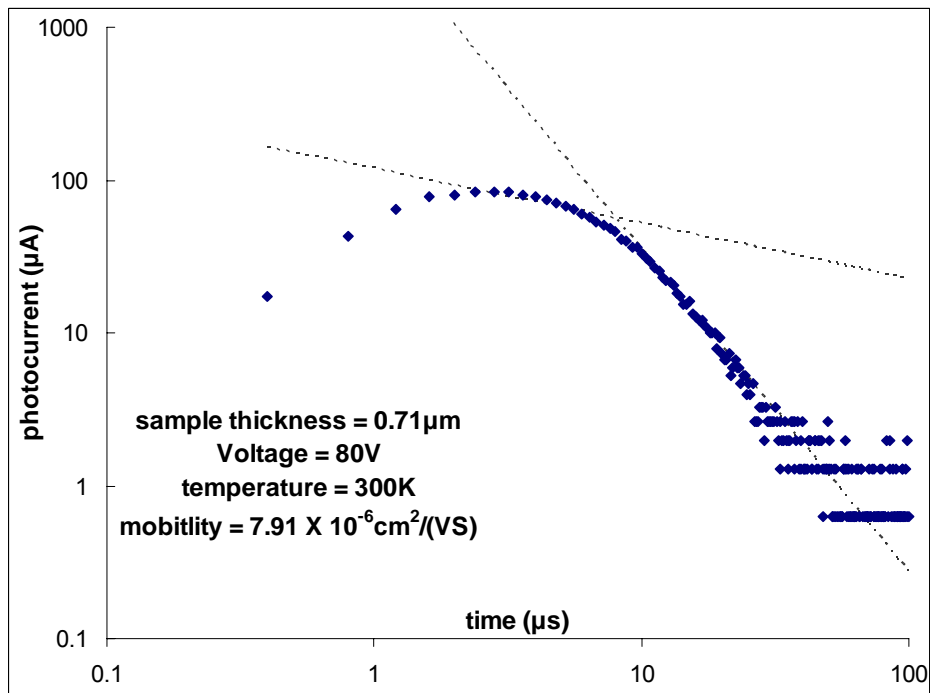


Figure 5.8 TPA-Cz3d: Log-Log plot of the photocurrent for 80V.

$$\alpha_{initial} = 0.64, \alpha_{final} = 1.11 \text{ and the transit time (intersection) is at } 7.97 \mu s.$$

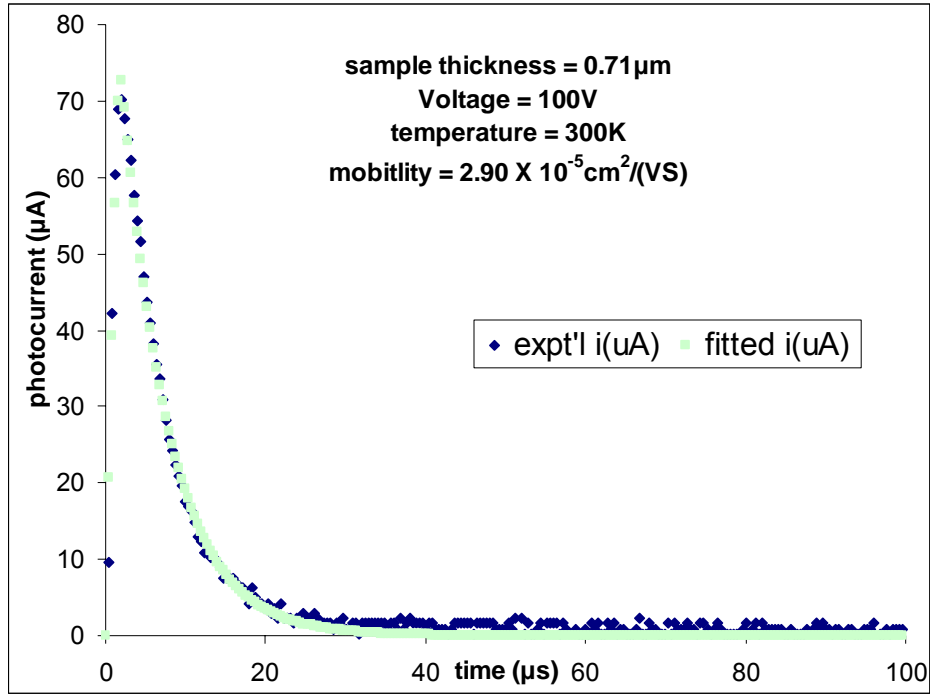


Figure 5.9 TPA-Cz3d: Experimental and fitted photocurrent for 100V.

$$\tau = 5.97 \mu\text{s}, \sigma_0 = 0.0890 \text{ m/s}, v_0 = 0.408 \text{ m/s}, q_0 = 538 \text{ pC}$$

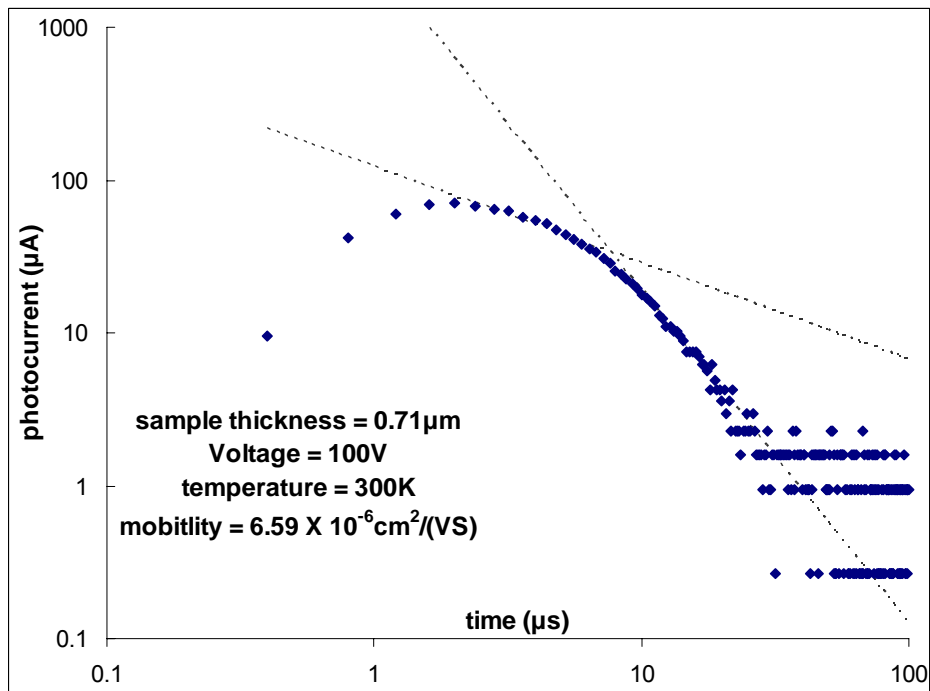


Figure 5.10 TPA-Cz3d: Log-Log plot of the photocurrent for 100V.

$$\alpha_{initial} = 0.37, \alpha_{final} = 1.17 \text{ and the transit time (intersection) is at } 7.65 \mu\text{s}.$$

## 5.2 ANTH-OXA6t-OC12

The electron mobilities for device ITO/Se(30nm)/ANTH-OXA6t-OC12 (0.9 $\mu\text{m}$ )/Al(100nm), which are obtained by Zou's model and S-M model under different applied voltages at room temperature ( $\sim 300\text{K}$ ), are given below.

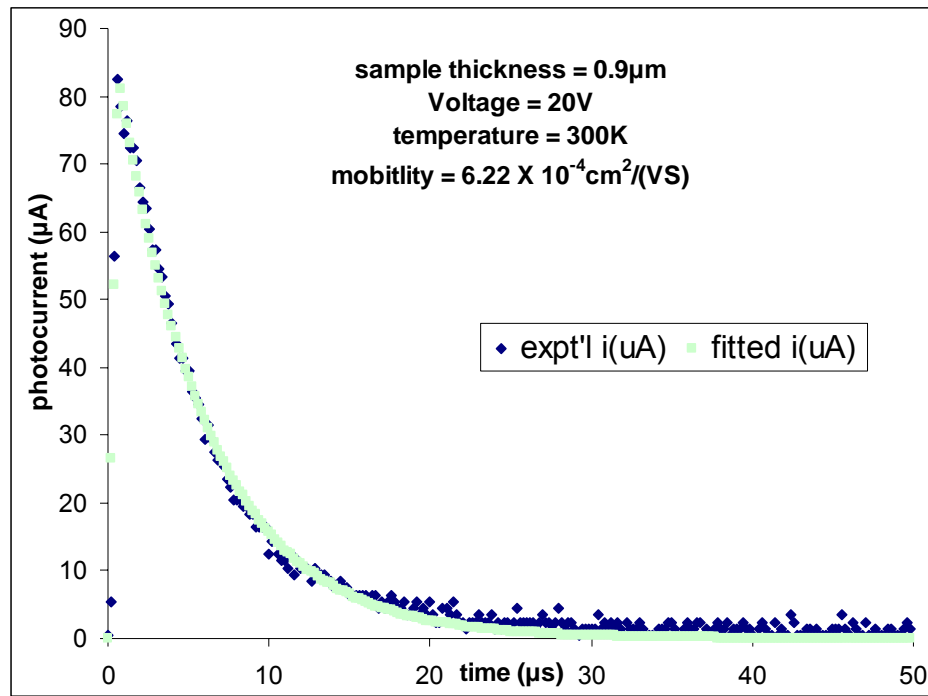


Figure 5.11 ANTH-OXA6t-OC12: Experimental and fitted photocurrent for 20V.

$$\tau = 5.76 \mu\text{s}, \sigma_0 = 0.0115 \text{m/s}, v_0 = 1.38 \text{m/s}, q_0 = 511 \text{pC}$$

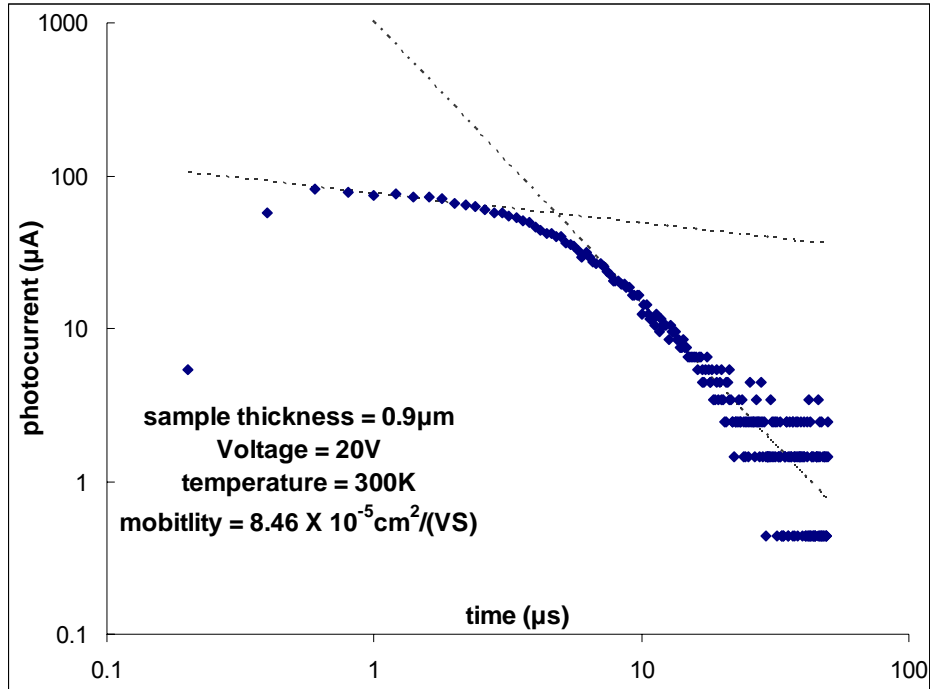


Figure 5.12 ANTH-OXA6t-OC12: Log-Log plot of the photocurrent for 20V.  
 $\alpha_{initial} = 0.81$ ,  $\alpha_{final} = 0.84$  and the transit time (intersection) is at  $4.78\mu s$ .

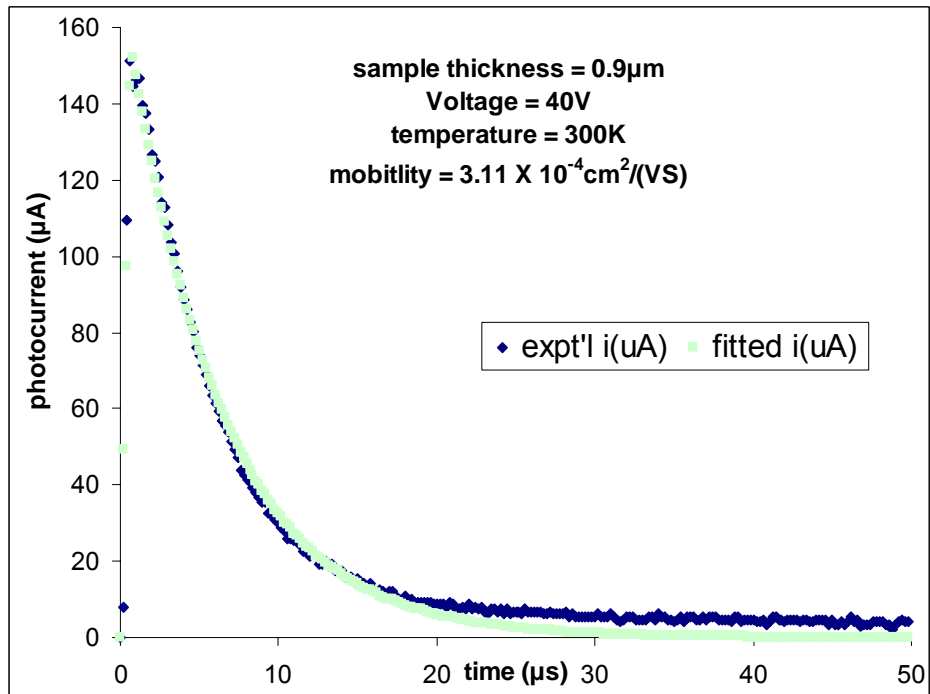


Figure 5.13 ANTH-OXA6t-OC12: Experimental and fitted photocurrent for 40V.  
 $\tau = 6.14\mu s$ ,  $\sigma_0 = 0.0122m/s$ ,  $v_0 = 1.38m/s$ ,  $q_0 = 1015pC$

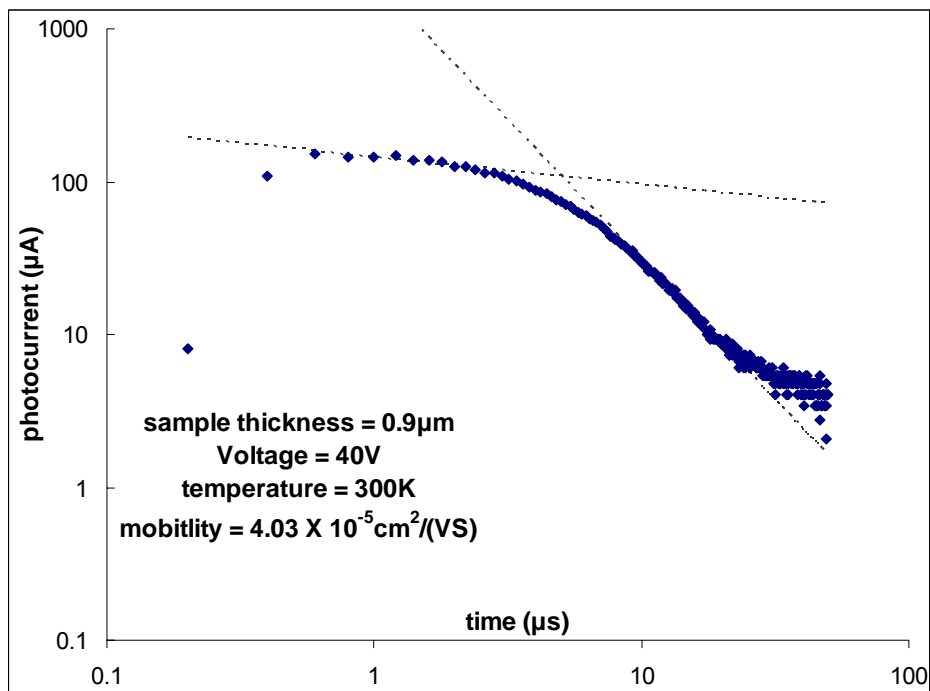


Figure 5.14 ANTH-OXA6t-OC12: Log-Log plot of the photocurrent for 40V.

$\alpha_{initial} = 0.82$ ,  $\alpha_{final} = 0.83$  and the transit time (intersection) is at  $5.02\mu s$ .

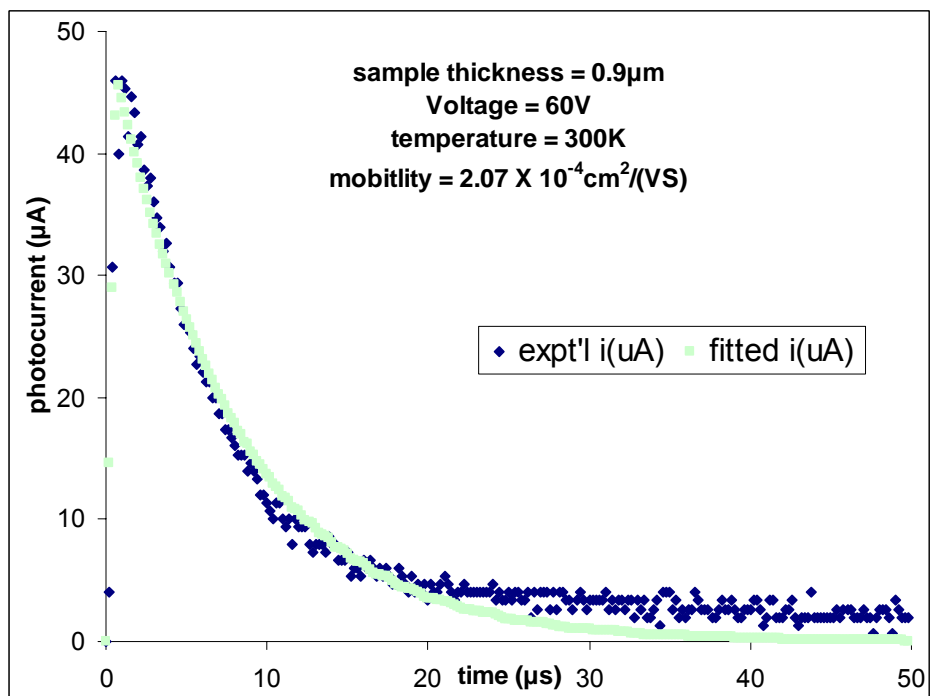


Figure 5.15 ANTH-OXA6t-OC12: Experimental and fitted photocurrent for 60V.

$\tau = 7.95\mu s$ ,  $\sigma_0 = 0.0107 m/s$ ,  $v_0 = 1.38 m/s$ ,  $q_0 = 387 pC$

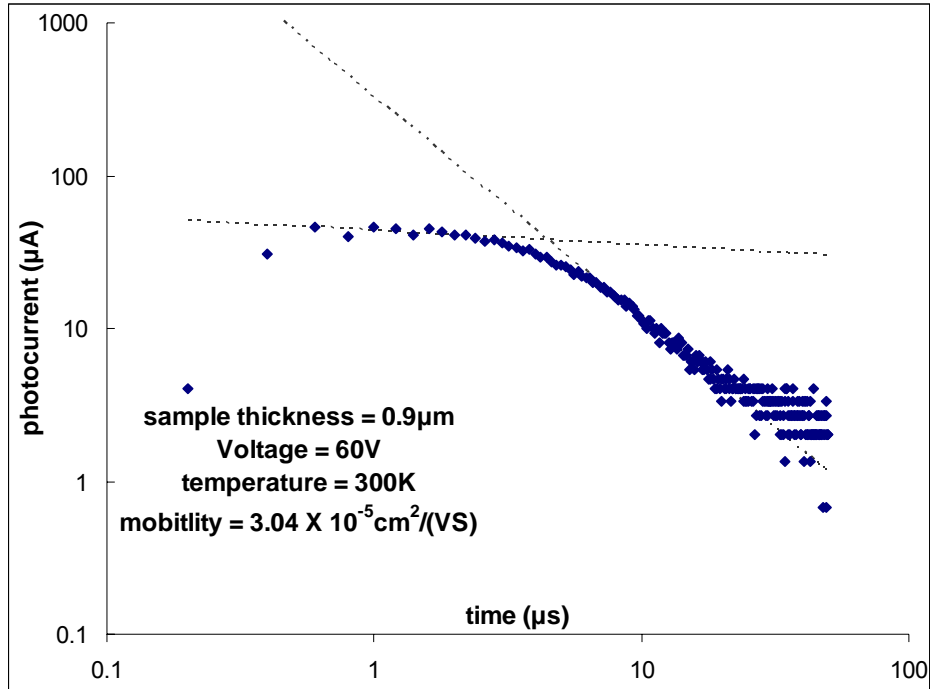


Figure 5.16 ANTH-OXA6t-OC12: Log-Log plot of the photocurrent for 60V.  
 $\alpha_{initial} = 0.90$ ,  $\alpha_{final} = 0.44$  and the transit time (intersection) is at  $4.45\mu s$ .

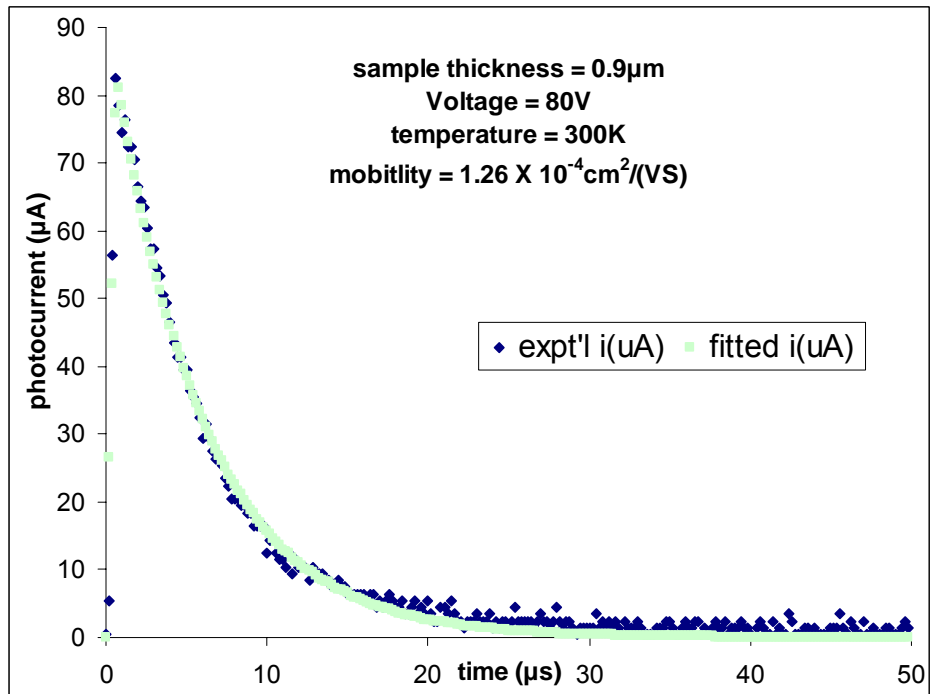


Figure 5.17 ANTH-OXA6t-OC12: Experimental and fitted photocurrent for 80V.  
 $\tau = 7.61\mu s$ ,  $\sigma_0 = 0.0996 m/s$ ,  $v_0 = 1.12 m/s$ ,  $q_0 = 994 pC$

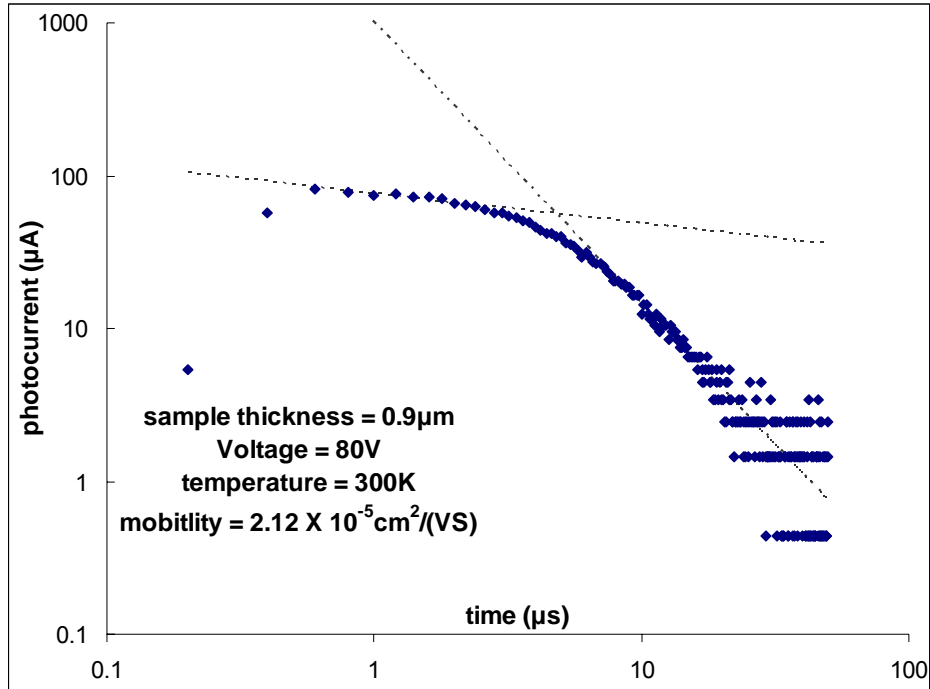


Figure 5.18 ANTH-OXA6t-OC12: Log-Log plot of the photocurrent for 80V.  
 $\alpha_{initial} = 0.81$ ,  $\alpha_{final} = 0.84$  and the transit time (intersection) is at  $4.78\mu s$ .

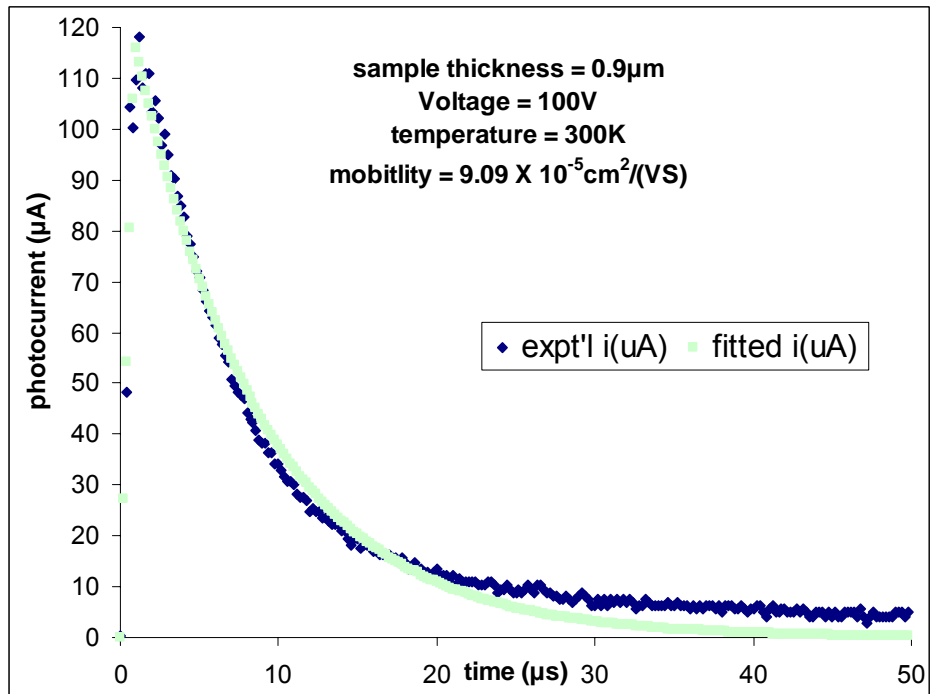


Figure 5.19 ANTH-OXA6t-OC12: Experimental and fitted photocurrent for 100V.  
 $\tau = 8.23\mu s$ ,  $\sigma_0 = 0.0202m/s$ ,  $v_0 = 1.01m/s$ ,  $q_0 = 1030pC$

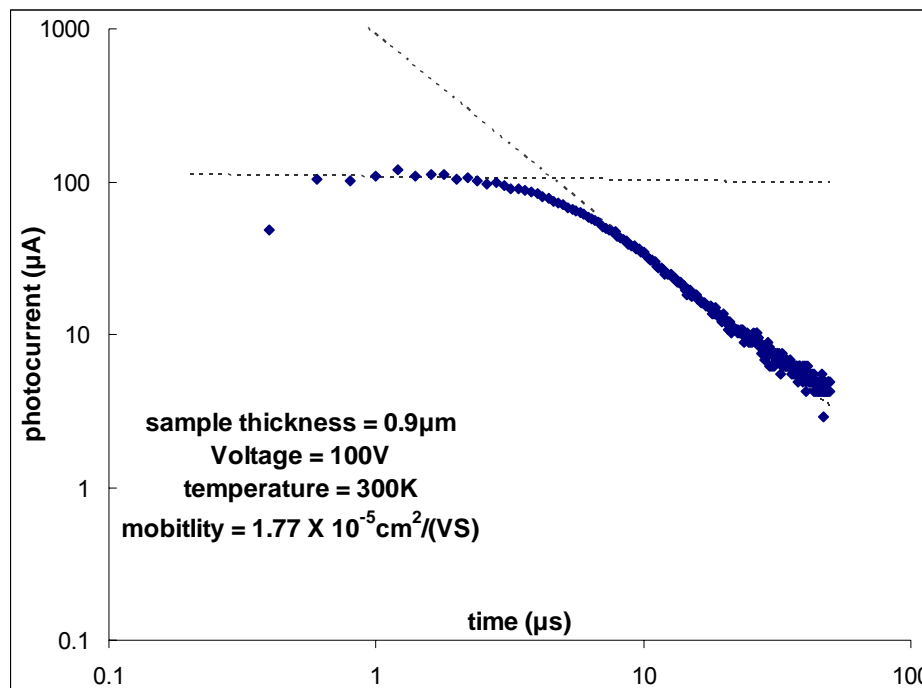


Figure 5.20 ANTH-OXA6t-OC12: Log-Log plot of the photocurrent for 100V.  $\alpha_{initial} = 0.98$ ,  $\alpha_{final} = 0.43$  and the transit time (intersection) is at  $4.58\mu\text{s}$ .

### 5.3 Discussions

From the above figures, we see that it is difficult to apply Scher-Montroll model to these materials. The transit time (intersection of two slopes) is not easy to be located. This might be due to the limitations of this model discussed earlier in section 4.3. Different researchers would possibly obtain different transit times for the same raw data by this method. Hence it is very hard to investigate the mobility properties quantitatively by this model.

On the other hand, the fitted photocurrent obtained by Xiaoming Zou's model is quite encouraging. It provides a way to obtain the so-called "average" mobility consistently and quantitatively for comparisons of all organic materials. However, this model needs much more experimental data to support. More

importantly, it needs agreements from some fundamental theory, such as quantum dynamics, to convince people that the mobility obtained by this model is reliable enough for quantitative applications.

## BIBLIOGRAPHY

1. J. Dresner, *J. Phys. Chem. Solids*, **25**, 505 (1964).
2. A.M. Goodman, *Phys. Rev.*, **164**, 1145 (1967).
3. H. Gobrecht, A. Tausend, and G. Clauss, *Z. Physik*, **176**, 155 (1963).
4. N.F. Mott and R.W. Gurney, *Electronic Processes in Ionic Crystals*, Oxford University Press 1940, New York, P.42
5. H. Bässler, *Phys. Status Solidi (b)*, **107**, 9 (1981).
6. Y. Hoshino, *J. Appl. Phys.*, **52**, 5655 (1981).
7. I. Glowacki, J. Ulanski, J. Sielski, and M. Kryszewski, *Synth. Met.*, **37**, 357 (1990).
8. H. Bässler, G. Becker, and N. Riehl, *Phys. Status Solidi*, **15**, 347 (1966).
9. A. Samoc, M. Samoc, and J. Swaorakowski, *Phys. Status Solidi (a)*, **36**, 735 (1976).
10. P.A.M. Dirac, *Proc. Roy. Soc. (London)*, **123**, 714 (1929).
11. J.C. Slater, *Phys Rev.* **34**, 1293 (1929).
12. L.H. Thomas, *Proc. Camb. Phil. Soc.*, **23**, 542 (1927).
13. E. Fermi, *Rend. Accad. Lincei.*, **6**, 602, (1927).
14. P.A.M. Dirac, *Proc. Camb. Phil. Soc.*, **26**, 376 (1930).
15. W. Kohn and L. Sham, *Phys. Rev.*, **140**. A1133 (1965).

16. P.J. Stevens, J.F. Devlin, C.F. Chabalowski and M.J. Frisch, *J. Phys. Chem.*, **98**, 11623 (1994).
17. M.E. Casida, K.C. Casida and D.R. Salahub, *Int. J. Quantum Chem.*, **70**, 933 (1998).
18. D.D. Gebler and Y.Z. Wang, *J. Chem. Phys.*, **108**, 7842 (1998).
19. Y.Z. Wang, D.D. Gebler, L.B. Lin, J.W. Blatchford, S.W. Jessen, H.L. Wang and A.J. Epstein, *Appl. Phys. Lett.*, **68**, 894 (1996).
20. Y.Z. Wang, D.D. Gebler, D.K. Fu, T.M. Swager and A.J. Epstein, *Appl. Phys. Lett.*, **70**, 3215 (1997).
21. J.A.O. Smallfield, *Metal-Polymer and Polymer-Polymer Interfaces: Application to Conjugated Polymer Electronic Devices*, PhD Dissertation, Physics Department at The Ohio State University (2002).
22. M. J. Frisch *et al*, Gaussian Inc., Pittsburgh PA, 1998.
23. A. J. Epstein *et al*, *Synth. Met.*, **78**, 253 (1996).
24. F.C. De Lucia, T.L. Gustafson, D.K. Wang and A.J. Epstein, *Phys. Rev. B*, **65**, 235204 (2002).
25. W.E. Spear, *J. Non-Cryst. Solids*, **1**, 197 (1969).
26. W.E. Spear, *App. Optics Supp.*, **3**, 8 (1969).
27. E.O. Schulz-DuBois, *Proceedings of the IEEE*, **57**, 1748 (1969).
28. G. Pfister and C. H. Griffiths, *Phys. Rev. Lett.*, **40**, 659 (1978).
29. S. Naka, H. Okada, H. Onnagawa, and T. Tsutsui, *Appl. Phys. Lett.*, **76**, 197 (2000).
30. Poole, H.H., *Phil. Mag.* **32**, 112 (1916).
31. Frenkel, J., *Phys. Rev.*, **54**, 647 (1938).
32. J.L. Hartke, *J. Appl. Phys.*, **39**, 4871 (1968).
33. K. Morgan and R. Pethig, *Nature*, **223**, 1969 (5205).

34. A. Ruediger, O.F. Schirmer, A.K. Kadashchuk, and Yu.A. Skryshevskii, *Europhysics Letters*, **57**, 592 (2002).
35. H. Bässler, *Philos. Mag. B*, **50**, 347 (1984).
36. N. Van Lien and B.I. Shklovskii, *Solid State Commun.*, **38**, 99 (1981).
37. L.B. Schein, A. Rosenberger, and S.L. Rice, *J. Appl. Phys.*, **60**, 4287 (1986).
38. A. Hirao, H. Nishizawa and M. Sugiuchi, *Phys. Rev. Lett.*, **75**, 1787 (1995).
39. D. Emin, *Phys. Rev. Lett.*, **32**, 303 (1974).
40. D.H. Dunlap, *Phys. Rev.*, **B52**, 939 (1995).
41. J.R. Haynes and W. Shockley, *Phys. Rev.*, **81**, 835 (1951).
42. R. Lawrence and A.F. Gibson, *Proc. Phys. Soc.*, **65B**, 994 (1952).
43. R.G. Kepler, *Phys. Rev.*, **119**, 1226 (1960).
44. O.H. LeBlanc, *J. Chem. Phys.*, **33**, 626 (1960).
45. A.V. Vannikov, *Sov. Phys. Solid State*, **9**, 1068 (1967).
46. M. Redecker, D.D.C. Bradley, and W. Wu, *Advanced Materials*, **11**, 241 (1999).
47. J. Haladyj, J. Michalski, and A. Szymanski, *Phys. Status Solidi A*, **80**, K137 (1983).
48. M. Redecker and D.D.C. Bradley, *Appl. Phys. Lett.*, **73**, 1565 (1998).
49. M. Pope and C.E. Swenberg, *Electronic Processes in Organic Crystals and Polymers*, Oxford University Press 1999, P.712.
50. J. Mort and P. Nielsen, *Phys. Rev. B*, **5**, 3336 (1972).
51. Soon-Wook Cha, *New Organic Luminescent Materials for OLEDs and Study for Photo-Induced Orientation of Polyoxetanes Containing Azo Chromophore*, PhD Dissertation, Chemistry Department at Korea University (2003).

52. F. Aramu, *Proceedings of the international conference on luminescence*, **1** and **2**, 1051 (1968).
53. P.M. Borsenberger and D.S. Weiss, *Organic Photoreceptors for Imaging Systems*, Marcel Dekker, Inc., 1993, P.280-281.
54. M.H. Cohen, *J. Noncrypt. Sol.*, **4**, 391 (1970).
55. J.M. Marshall, *Phil. Mag.*, **36**, 959 (1977).
56. H. Scher and E. W. Montroll, *Phys. Rev. B*, **12**, 2455 (1975).
57. G. Pfister, *Philos. Mag. B*, **36**, 1147 (1977).
58. H. Seki, *Proc. 5<sup>th</sup> Conf. On Amorphous and Liquid Semiconductors*, Garmish- Partenkirch, 1974, P.1015.
59. H. Bässler, *Phys. Stat. Sol. (B)*, **175**, 15 (1993).
60. S.M. Godson, and J. Hirsch, *Sol. Stat. Comm.*, **20**, 285 (1976).
61. H. Bässler, *Phys. Stat. Sol. (B)*, **175** 15 (1993).
62. J.C. Scott, L. Th. Pautmeier, and L.B. Schein, *Phys. Rev. B*, **46**, 8603 (1992).
63. Xiaoming Zou, *Models to Measure Mobilities By Time-Of-Flight*, PhD Dissertation, Physics Department at The Ohio State University (2002).
64. J. Noolandi, 7<sup>th</sup> Int. Conf. Amorph. and Liquid Semiconductors, Edinburgh, 1977, P.98.
65. J. C. Scott; T. Pautmeier; and L. B. Schein, *Physical Review B*, **46** , 8603, (1992).
66. U. Wolf, V. I. Arkhipov, and H. Bassler, *Physical Review B*, **59**, 7507, (1999).
67. H. Bassler, H. Rost, and H. H. Horhold, *Journal of Chemical Physics*, **113**, 3802, (2000).